

Figure 6.104: Morphology observations of cells seeded on P20 cement after 72 hours of cultivation

Figures 6.103 and 6.104 report the tendency of the cells to generate a new structure on the sample surface (evidenced with a red line). Analog behavior is observed in figures 6.105, 6.106 and 105.

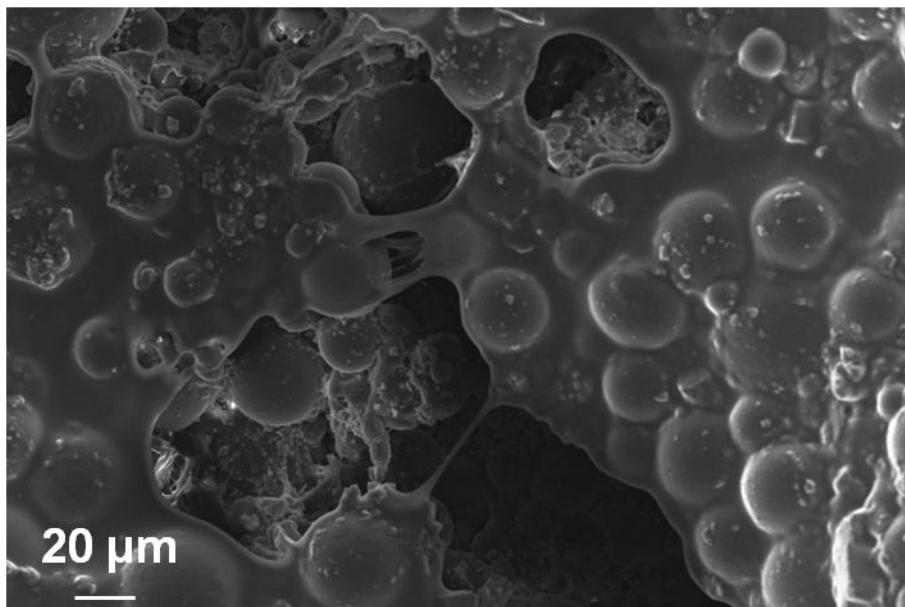


Figure 6. 105: Morphology observations of cells seeded on P20 cement after 72 hours of cultivation

Results and Discussion Composite bone cement characterization

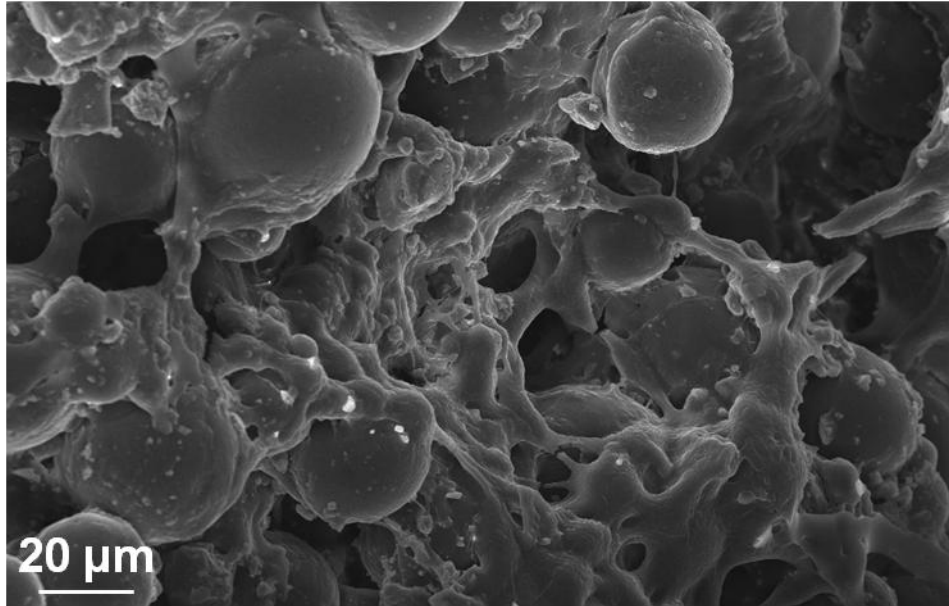


Figure 6. 106: Morphology observations of cells seeded on P20 cement after 72 hours of cultivation

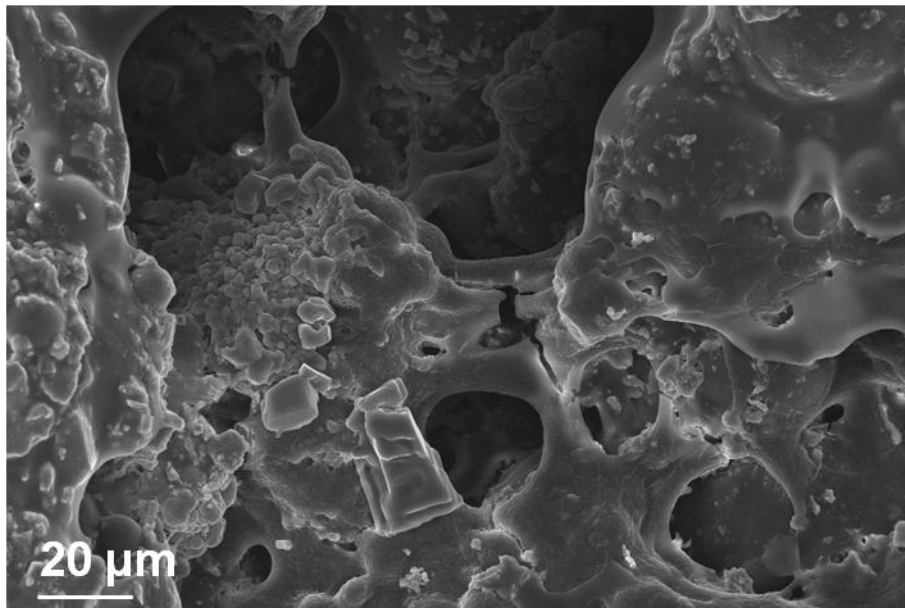
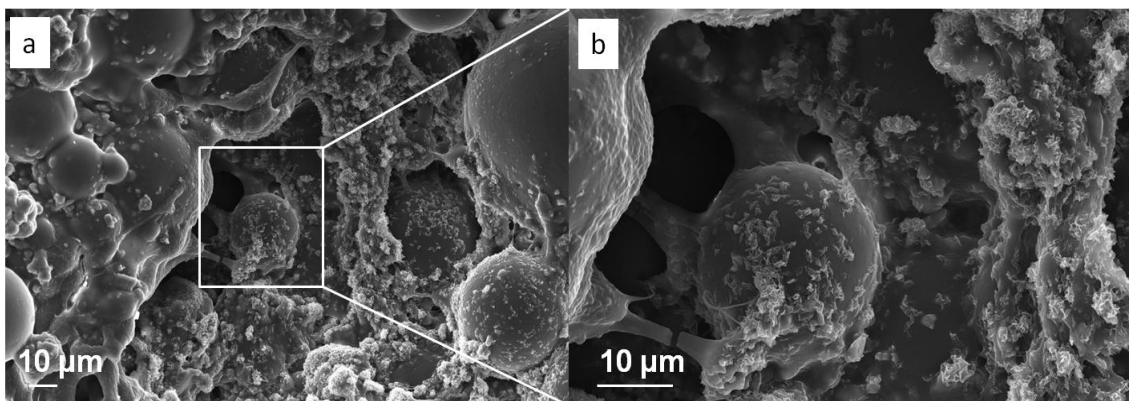


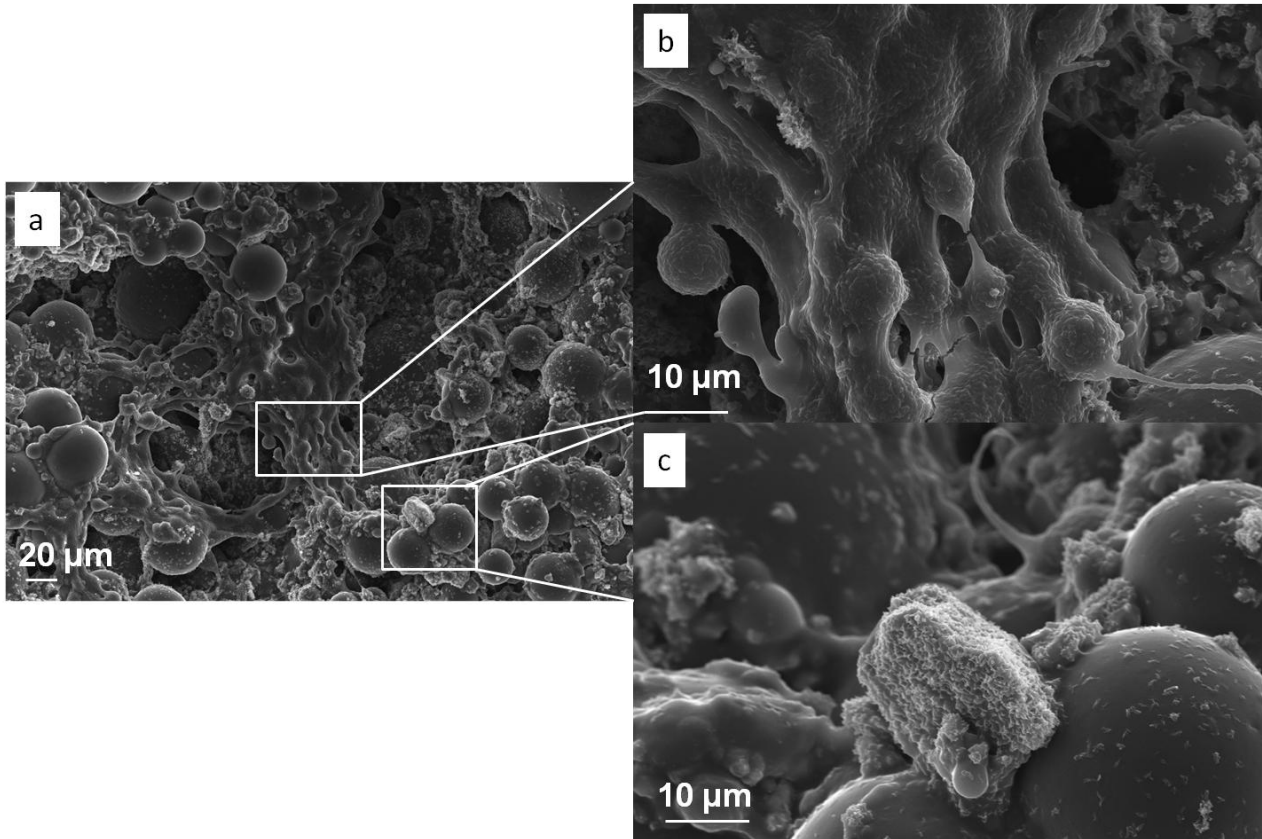
Figure 6. 107: Morphology observations of cells seeded on P20 cement after 72 hours of cultivation



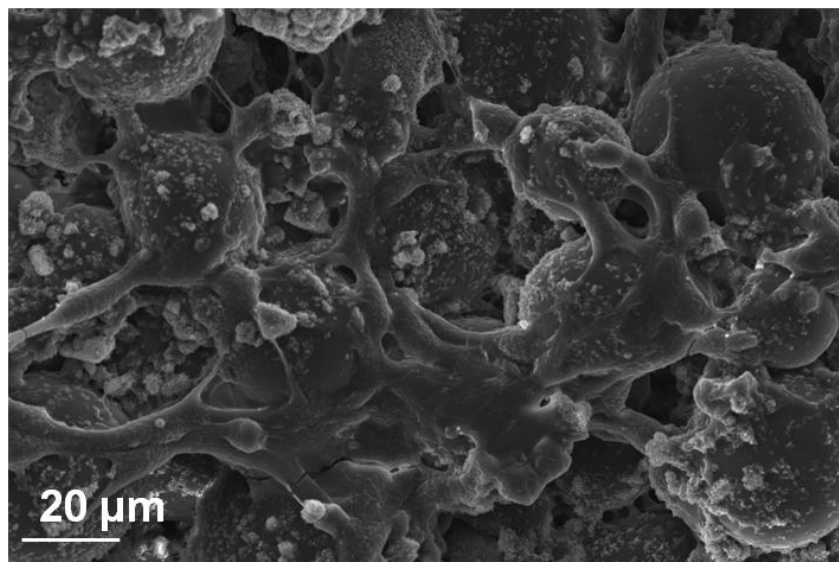
6.106: Morphology observations of calcium phosphate precipitates on P20 cement after 48 hours of cells cultivation

Results and Discussion Composite bone cement characterization

The presence of many precipitates of calcium and phosphorus are noticed even on P20 at 48 hours from cells seeding. The shape and morphology of the precipitates are associated to hydroxyapatite precursors. Figures 6.108a-b and 6.109 and 6.110 report many different precipitates in every part of the surfaces. An extremely good combined activity of bioactive composition of glass ceramic with the metabolic of cells are evaluated even on this sample.



6. 107: Morphology observations of calcium phosphate precipitates on P20 cement after 48 hours of cells cultivation



6. 108: Morphology observations of calcium phosphate precipitates on P20 cement after 48 hours of cells cultivation

Results and Discussion Composite bone cement characterization

The HAp precipitates precursor are seen on P10 and P20 at 48 hours from seeding and at 72 and 24 hours for P15. In any case these data are collected at a very early time-point (up to 72 hours), considering that the material itself is able to promote mineralization in the acellular SBF only after 28 days (as already reported from figure 6.37 to 6.44). The high amount of precipitates covering cells surface at a such early stage suggest a synergistic effect between the bioactivity of the material and cell activity, where cells seem to be stimulated in their mineralization process. Moreover, the same test performed soaking each sample into the culture medium without cells (data not shown) up to 72 hours did not reveal the formation of this type of precipitates, supporting this hypothesis. This result represents a very important starting point for a future clinical application of the investigated bone cements as materials for bone surgery.

Another very important behavior which is noticed on all the sample surface at 48 and 72 hours from cells seeding is its organization, which is often characterized by a tridimensional structure and several cells produced a highly interconnected tissue-like multilayered network. This topic is widely discussed in literature [17], where it is reported that this morphology is associated to enhanced pro-osteogenic activity. This feature is much less evident on the plain cement (pure Palamed[®], data not shown), due to its bio inert properties.

6.2.16. Preliminary in vitro heating test

In vitro cellular heating tests are performed using MG63 osteosarcoma and HFOB Human Fetal Osteoblast cells directly seeded on P10 and Palamed[®] sample. The first type of cells is tumoral while the second is healthy. In the previous test MG63 are used to evaluated the cytocompatibility material response while in this second characterization are used as tumoral cell line.

Figure 6.111 reports the results of MG63 and HFOB cell viability in contact with P10 and Palamed[®] specimens. Data show a good value of biocompatibility for tumoral and healthy cells. Higher values of optical density is evaluated for MG63 due to the higher doubling capacity respect to the HFOB. In any case optical density value is higher on P10 with HFOB and MG63 respect to Palamed[®]. This result confirms an higher level of cytocompatibility for P10 respect to Palamed[®] which is an inert material.

Results and Discussion Composite bone cement characterization

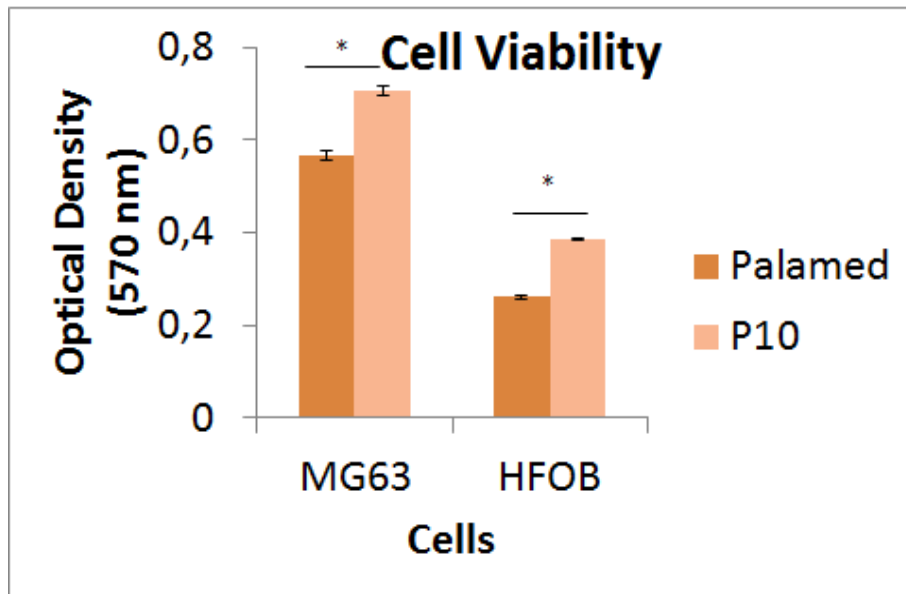


Figure 6.109: Cells viability on Palamed® and P10 specimens. A significant difference was noticed between P10 and Palamed® ($p < 0.005$, indicated by *) using MG63 and HFOB.

Moreover the obtained result is in agreement with the viability of cytocompatibility tests and confirms the positive presence of the SC45.

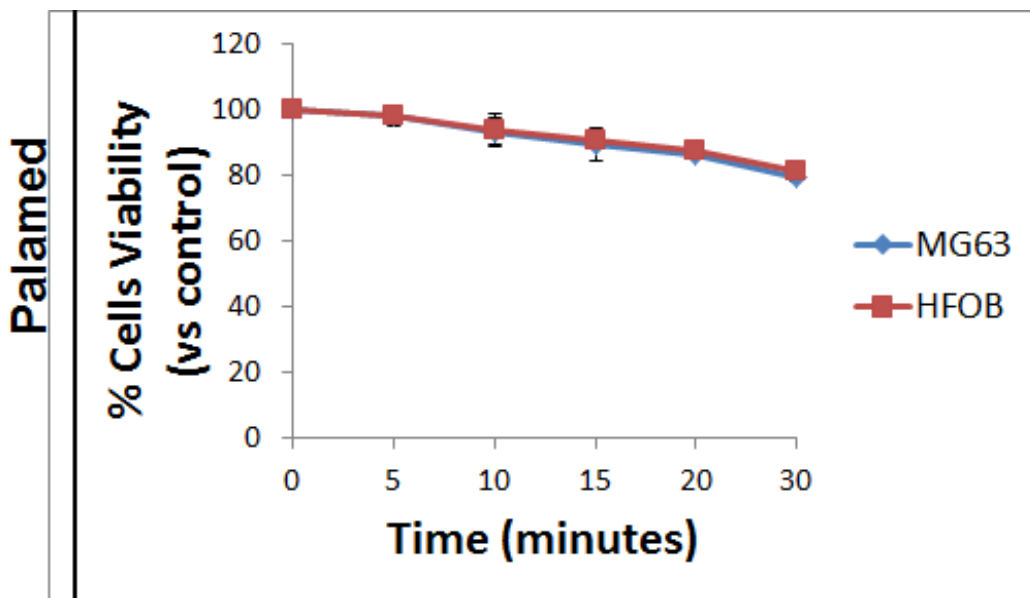


Figure 6.112: Effect of magnetic induction heating on Palamed® sample after 30 minutes

Figure 6.112 reports the effect of magnetic induction heating for the control sample (Palamed®). The trend of MG63 and HFOB viability is flat and overlap one on another. The lack of magnetic effect obstructs any decreasing of the tumoral cell viability.

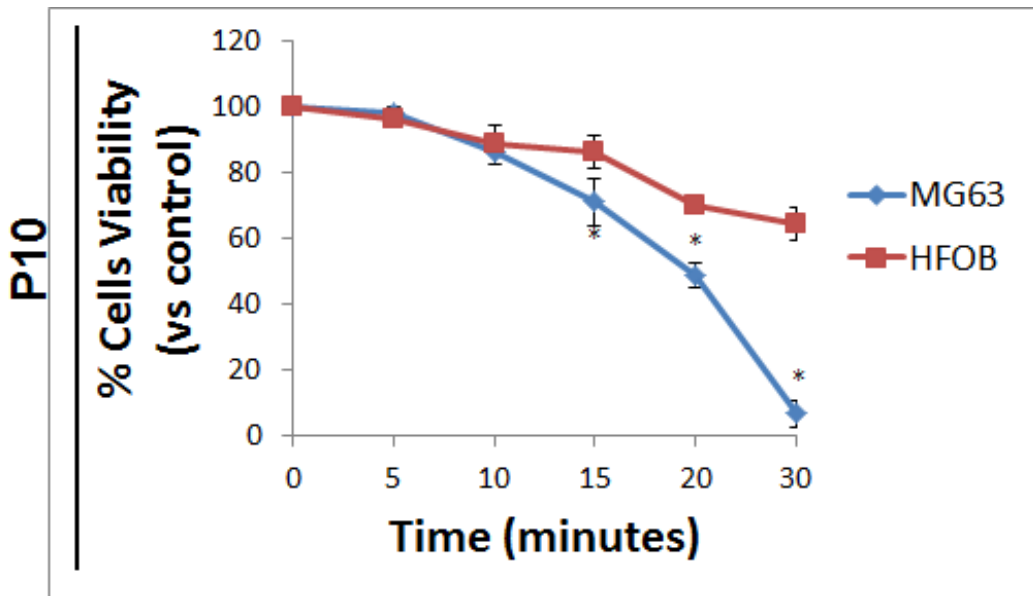


Figure 6.113: Effect of magnetic induction heating on P10 sample up to 30 minutes

In figure 6.113 is reported the effect of a magnetic induction heating on the viability of MG63 and HFOB cells for P10 samples. Results show a reduction of viability of tumoral cells (MG63) seeded on P10 in comparison to healthy ones (HFOB). In fact after 30 minutes the viability of tumoral cells decreases of 97%. While the value of HFOB slightly decreases but only of about 30%. This is a very important characterization because first of all it demonstrates the efficiency of the material and then that tumoral cells are much more sensible to heat generated by an external source respect to HFOB. This happens because MG63 cells have a genetic evolution that skip main cellular cycle control. For this reason tumoral cells are much more subject to go in apoptosis, when the surrounded temperature became too high for their surviving. To obtain this result it is sufficient to reach a temperature between 40°C and 44 °C typical of magnetic hyperthermia.

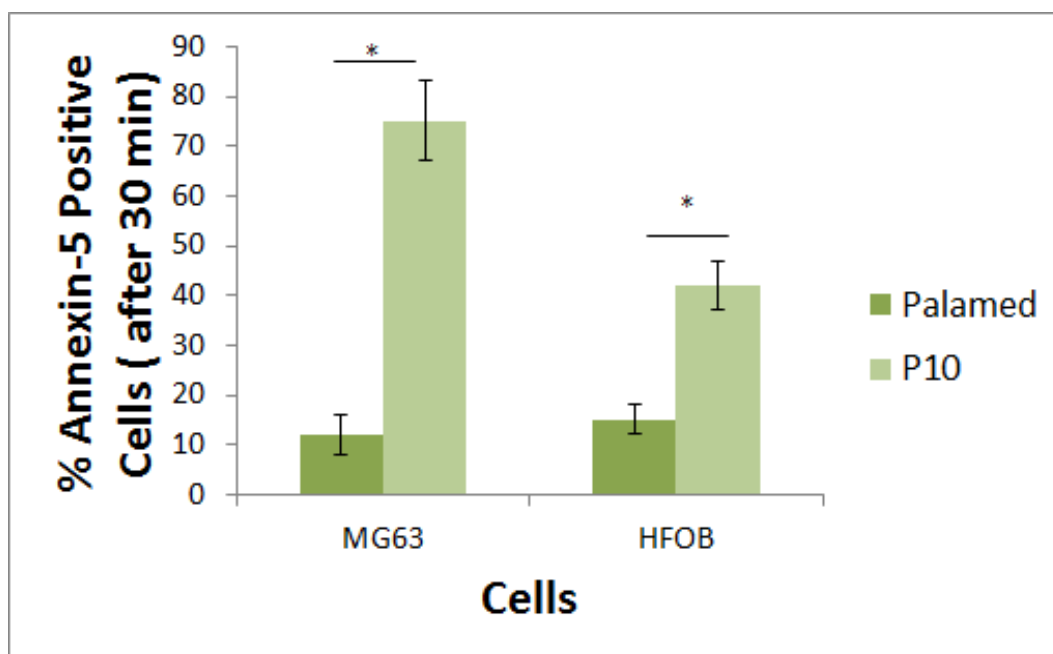


Figure 6.114: Annexin-5 positive cells test after 30 minutes of heating

Programmed cell death is evaluated with annexin-5 positive cells (figure 6.114) that evidences an high amount of apoptosis for MG63 on a magnetic sample. This is a further encouraging results because it indicates that the use of an external source of heat generates a death for MG63 without creating any necrosis phenomena with any damaging of HFOB cells .

Data from the literature [19] report that cell stimulation with heat generates an oxidative stress, which creates an increase rate of reactive oxygen species (ROS) and damages DNA, protein and lipids. The evidence of an elevate level of oxidative stress could be potentially dangerous for proteins and the up-regulation of heat shock protein (HSP) is required to restore their native structure. The activation of cellular repair mechanism and increased HSP and antioxidant production may help to repair the stress-induced cellular damage. It is possible that the mentioned theory could be applicable even in this case, where the better protection and cellular repair mechanism was express by HFOB cells and practically absent in MG63.

A morphological evaluation of MG63 and HFOB cells was performed before and after magnetic induction heating on P10 sample.

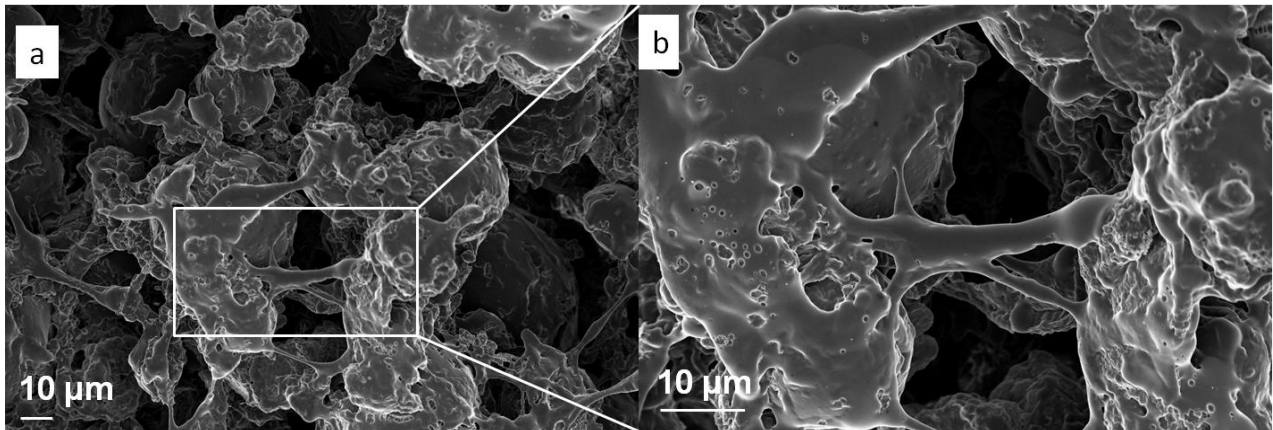


Figure 6.115: Morphological analysis of Human Fetal osteoblast (HFOB) on P10 before heating

Figure 6.115 reports the HFOB on P10 sample before magnetic heating. Cells appear very well spread with a flat morphology. Many connections are developed with the material and the other cells. An elevated level of cytocompatibility is observed even for HFOB.

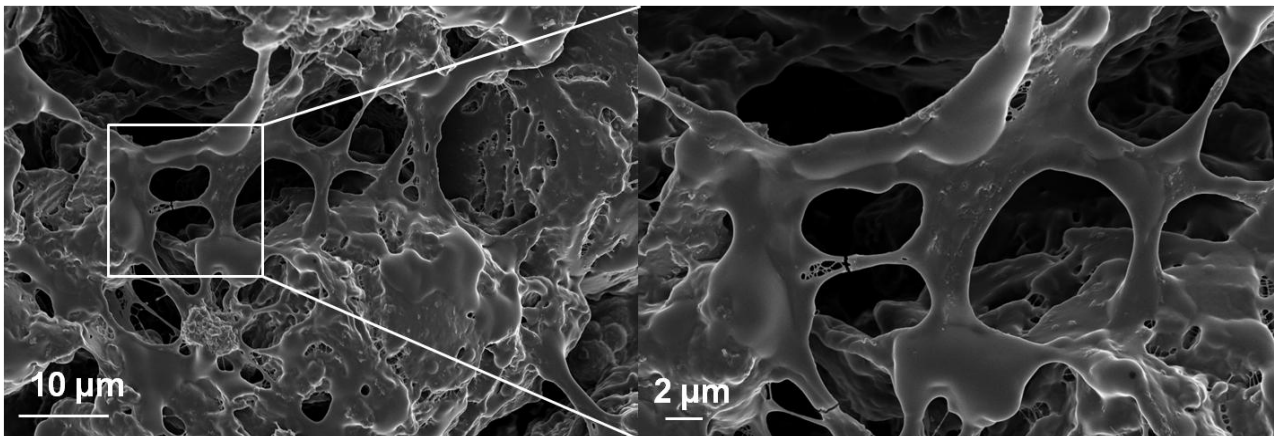


Figure 6.116: Morphological analysis of Human Fetal osteoblast (HFOB) on P10 before heating

Figure 6.116 reports a very interconnected morphology of HFOB cells on P10 sample.

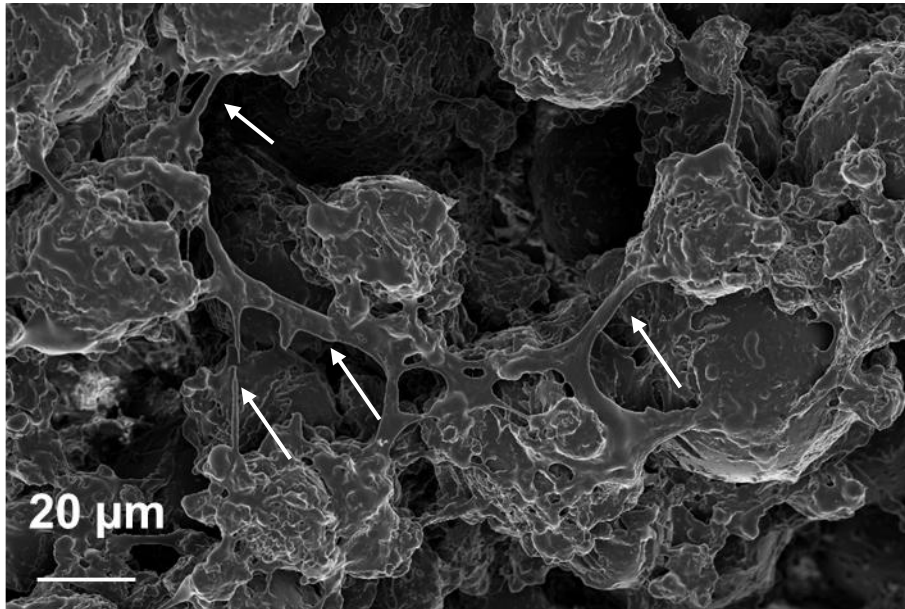


Figure 6.117: Morphological analysis of Human Fetal osteoblast (HFOB) on P10 before heating

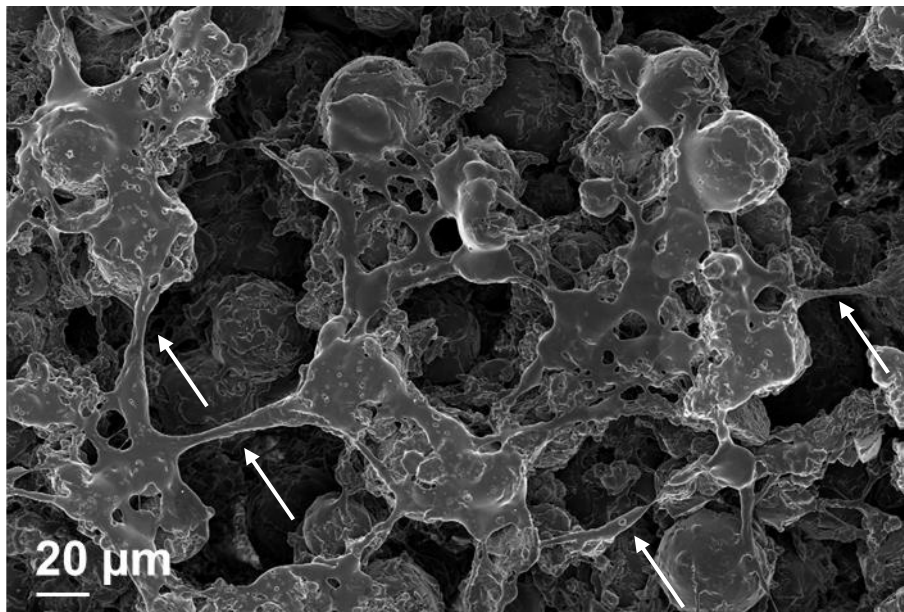


Figure 6.118: Morphological analysis of Human Fetal osteoblast (HFOB) on P10 before heating

Figures 6.117 and 6.118 evidence the morphology of HFOB very well spread on the surface of P10. Many bridging like structure are observed and indicated by the arrows.

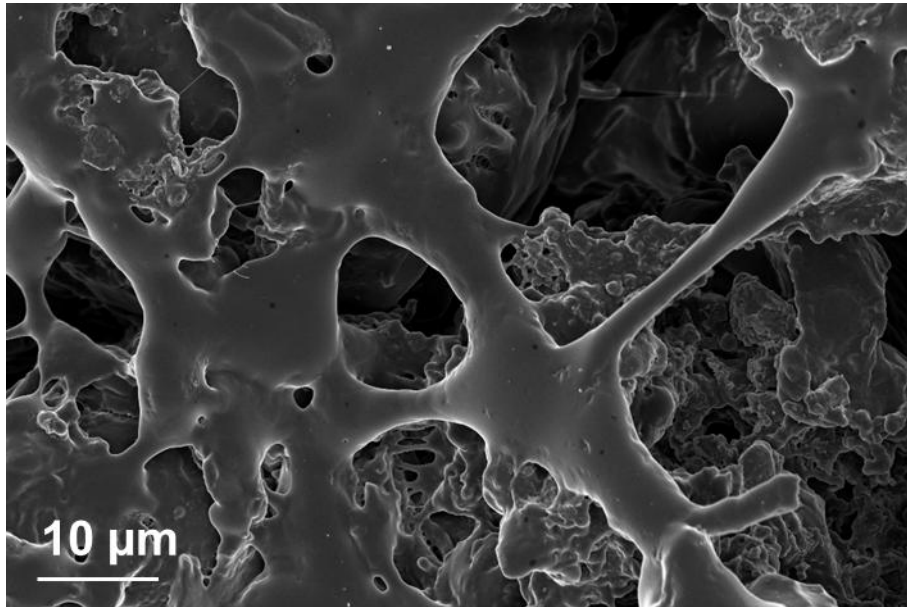


Figure 6.119: Morphological analysis of Human Fetal osteoblast (HFOB) on P10 before heating

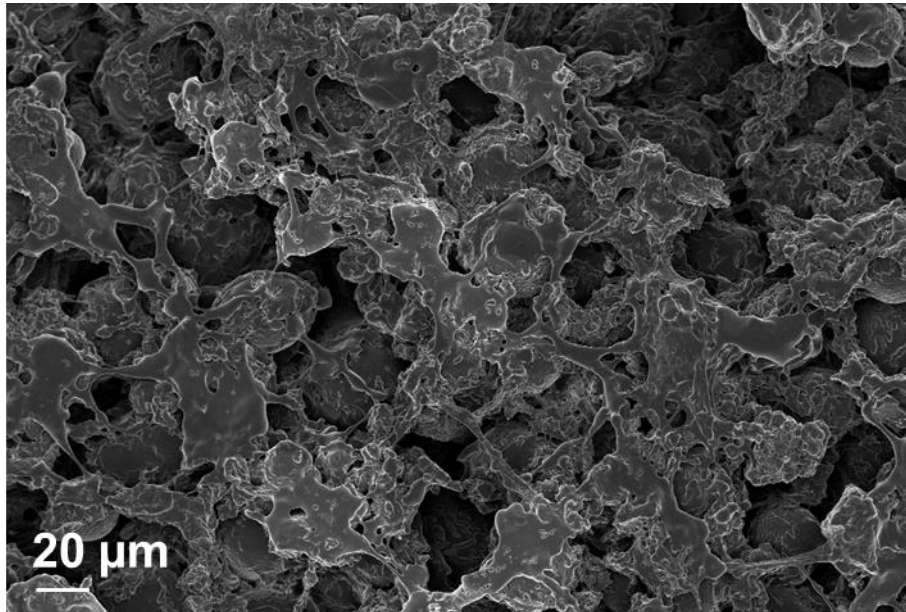


Figure 6.120: Morphological analysis of Human Fetal osteoblast (HFOB) on P10 before heating

Figures 6.119 and 6.120 show other similar morphology of HFOB on P10 sample.

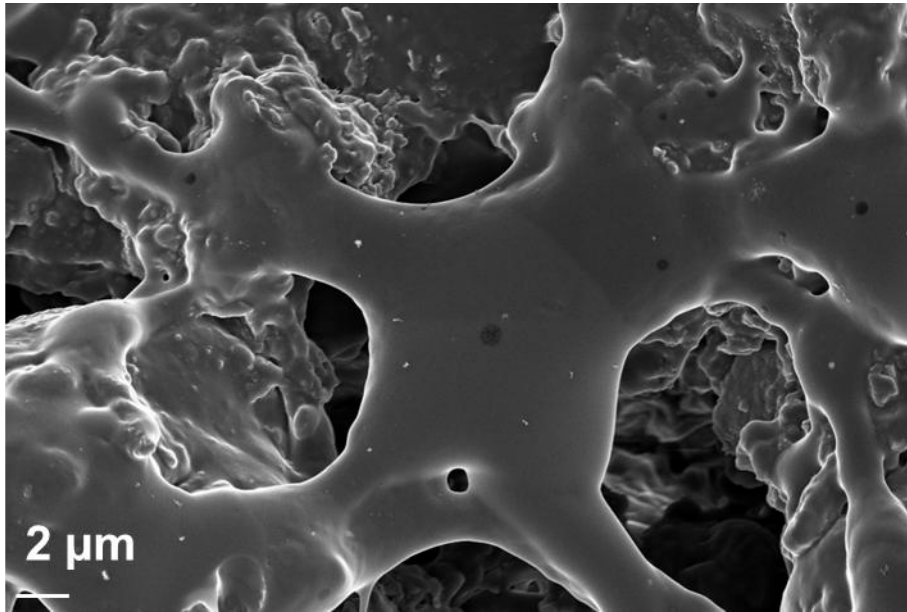


Figure 6.121: Morphological analysis of Human Fetal osteoblast (HFOB) on P10 before heating

Figure 6.121 reports a magnification of HFOB flat morphology. It can be affirmed that the human fetal osteoblast adhere and proliferate very well on the P10 surface. The morphological results are in agreement with cell viability.

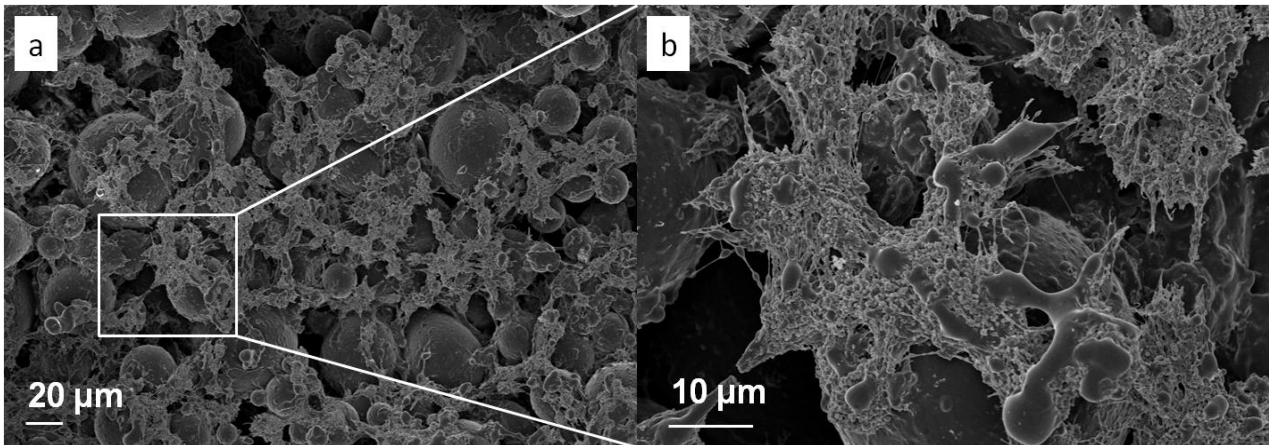


Figure 6.122: Morphological analysis of osteosarcoma cells(MG63) on P10 before heating

Figure 6.122 reports morphological analysis of MG63 on P10 samples before heating. The shape and size of these cells are very different from HFOB.

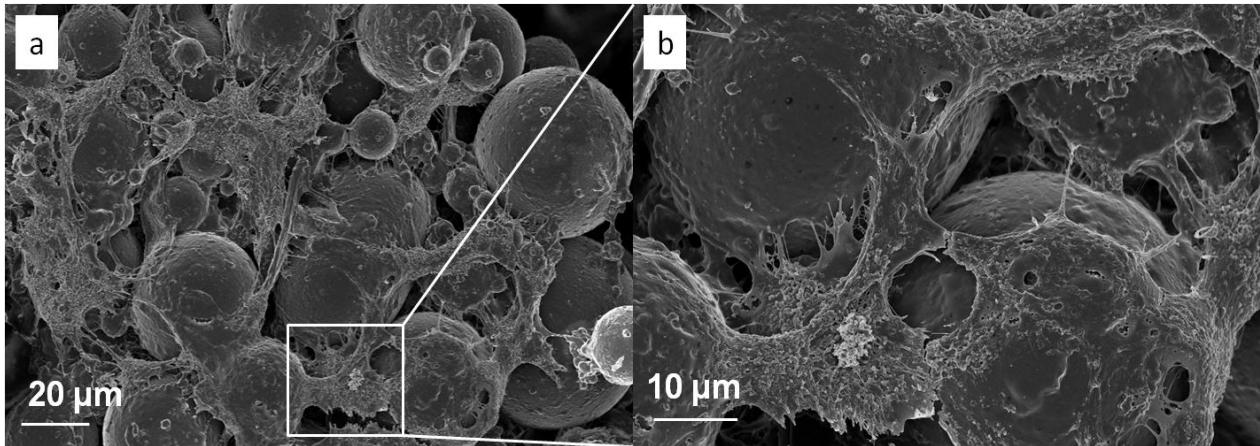


Figure 6.123: Morphological analysis of osteosarcoma cells (MG63) on P10 before heating

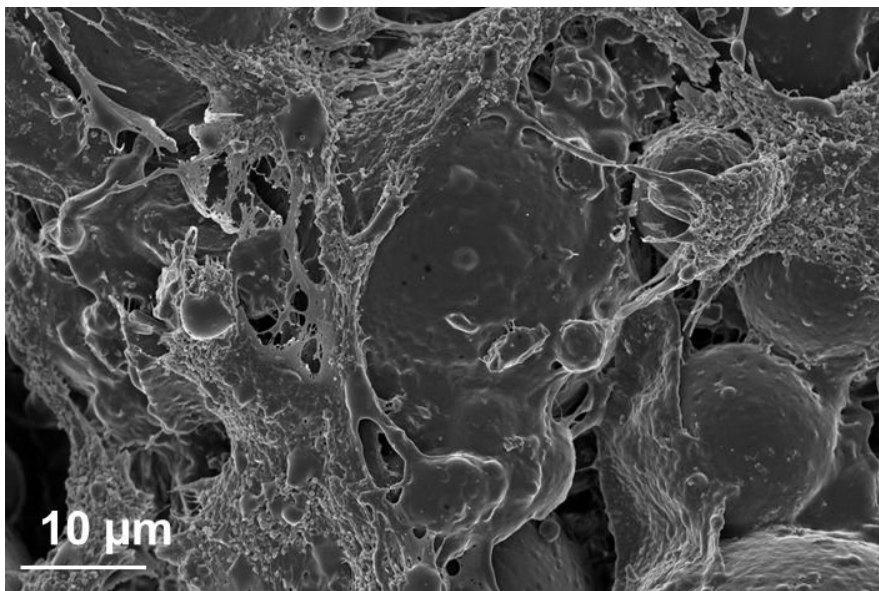


Figure 6.124: Morphological analysis of osteosarcoma cells(MG63) on P10 before heating

Figures 6.123 and 6.124 report an high value of cellular interconnections and adhesion on the biomaterial.

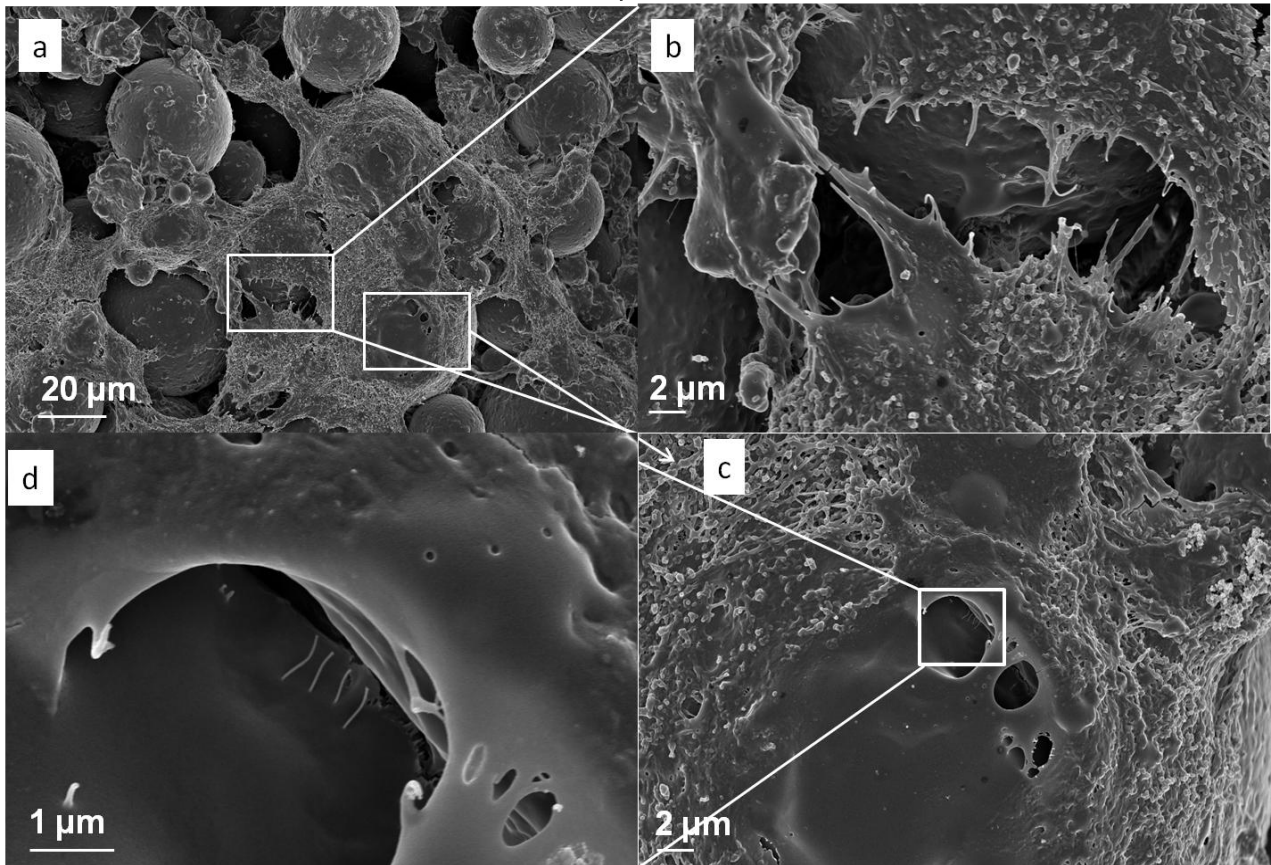


Figure 6.125: Morphological analysis of osteosarcoma cells(MG63) on P10 before heating

Figure 6.125 reports a panel in which three different magnification of cells are visible. In figure 6.125b a scratch with two side of cells is observed , in figure 6.125b a spherical PMMA particle is completely cover by MG63 and in figure 6.125d a detail of an hole created by a cell.

After the evaluation of cellular morphology of MG63 and HFOB it is reported the morphology investigation of the same cells after 30 minutes of magnetic induction heating. The inductive magnetic furnace generates a magnetic field of 22,5 mT at a fixed frequency of 220 kHz. Heating is performed on triplicate samples .

Results and Discussion Composite bone cement characterization

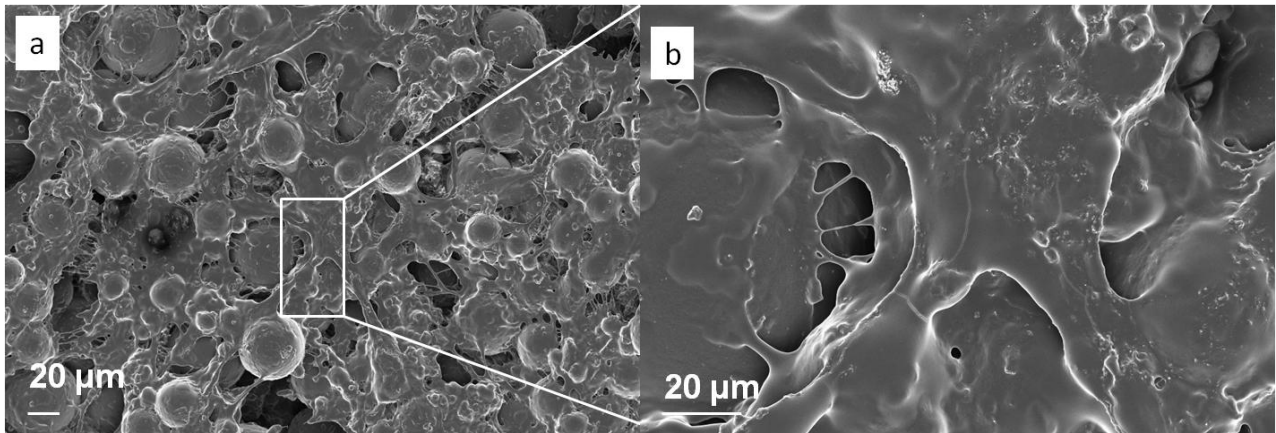


Figure 6.126: Morphological analysis of HFOB on P10 after 30 minutes of heating

Figure 6.126 reports the HFOB morphology after 30 minutes of heating. It can be assessed any change of cellular structure respect to the same cell line before heating.

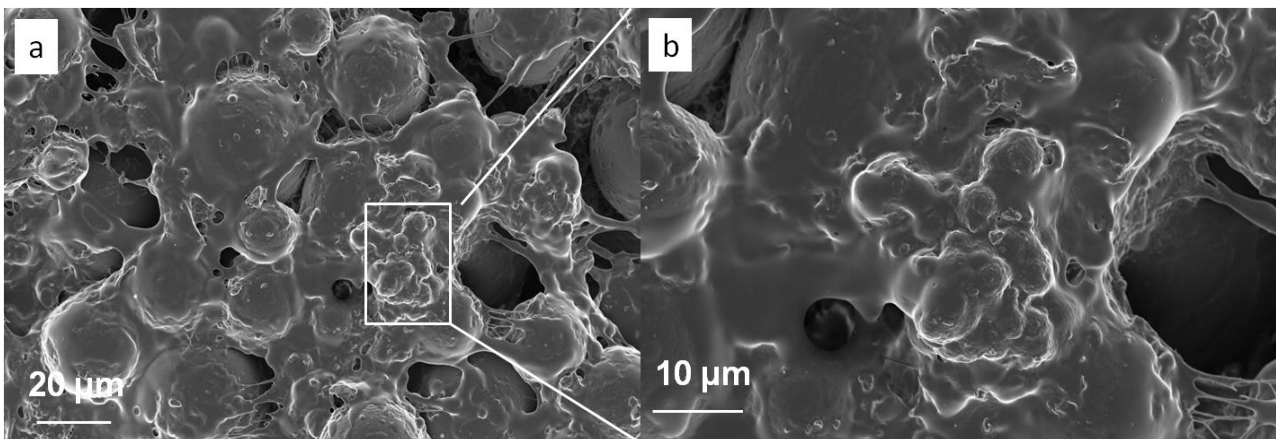


Figure 6.127: Morphological analysis of HFOB on P10 after 30 minutes of heating

Figure 6.127 evidences some human fetal osteoblasts in apoptosis; in fact the morphology of cells change and the cellular body tend to shrink.

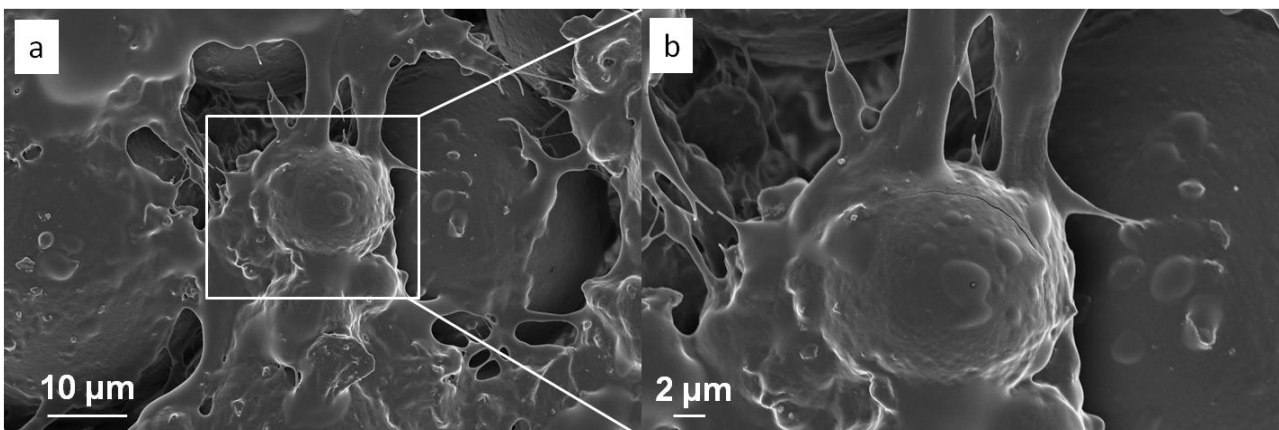


Figure 6.128: Morphological analysis of HFOB on P10 after 30 minutes of heating

Results and Discussion Composite bone cement characterization

Figure 6.128 reports an apoptosis of HFOB .The cell evidences with a white square is subjected to a shrinkage with a consequent separation from the other. The cell programs its death detaching from the other. This particular condition is observed only on a few zone of analyzed sample.

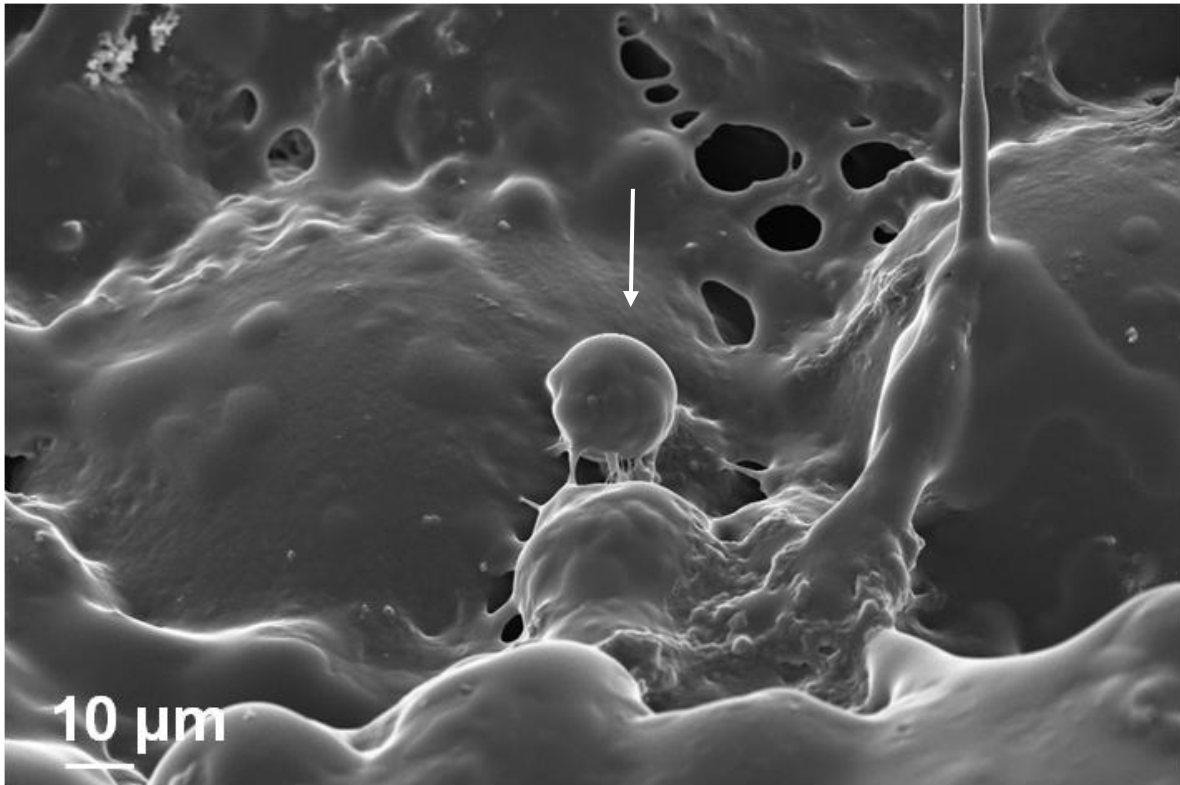


Figure 6.129: Morphological analysis of MG63 on P10 after 30 minutes of heating

The most important results is evaluated in figure 6.129 where it visible the heating of MG63 on P10 sample. The arrows indicate the clearly presence of a cell which programmed its death. It can be seen the absence of cellular connection and a high level of shrinking respect to the other cells.

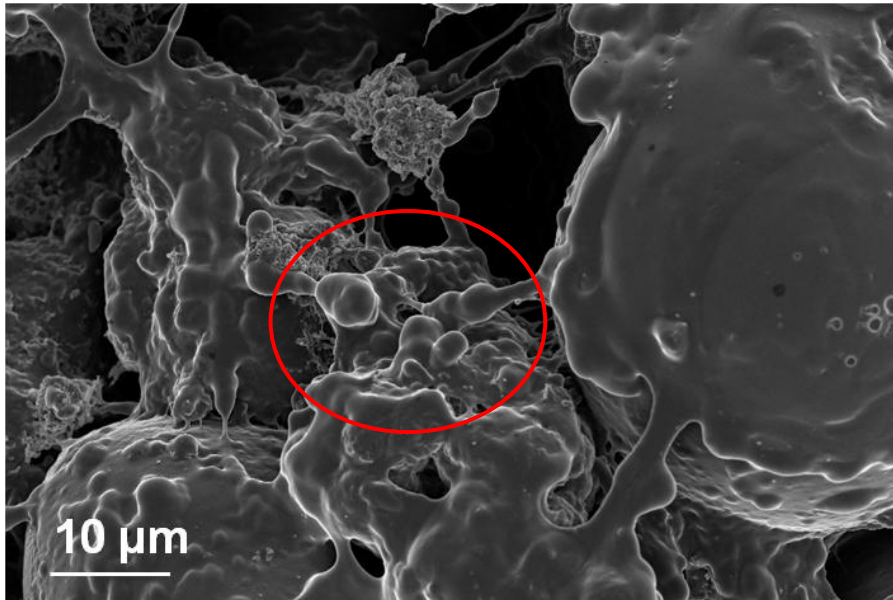


Figure 6.130: Morphological analysis of MG63 on P10 after 30 minutes of heating

Similar behavior can be assessed in figure 6.130 as shown with the cells in the red circle.

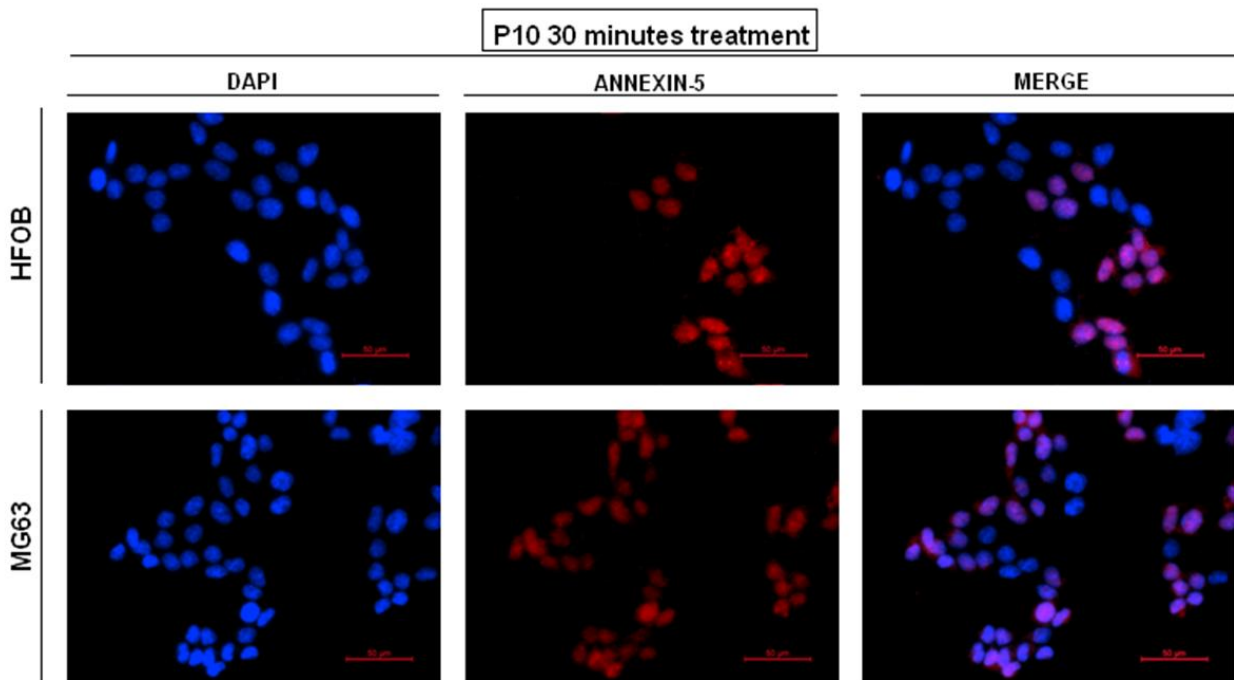


Figure 6.131: Colorimetric evaluation of cellular nuclei of HFOB and MG63 after 30 minutes of heating on P10 sample

Figure 6.131 reports a colorimetric evaluation of MG63 and HFOB cellular nuclei. On the left column is reported the total quantity of cells (dapi). All the nuclei are evidenced in blu for MG63 and HFOB. In the central images the red color evidences all cells in apoptosis. In agreement with

Results and Discussion Composite bone cement characterization

the viability test the number of cells is higher for MG63 than that HFOB after 30 minutes of heating. The merge images represent the overlap of the two previous results and it can be evidenced an higher number of MG63 violet cells (indicating the cells that program their apoptosis) respect to HFOB with a consequently higher apoptosis for tumoral cell line.

6.3. Reference

1. Bretcanu O, Verné E, Cöisson M, Tiberto P, Allia P, Magnetic properties of the ferrimagnetic glass-ceramics for hyperthermia, *J Magn Magn Mater* 2006; 305: 529-533.
2. Bretcanu O, Spriano S, Brovarone VC, Vernè E, Synthesis and characterization of coprecipitation-derived ferrimagnetic glass-ceramic, *J Mater Sci* 2006; 41: 1029-1037.
3. Bretcanu O, Ferraris S, Miola M, Vernè E, *Adv in Bioc and Biotech: Cer Trans*, New York: Wiley & Sons; 2012: 139-144.
4. Jallot E, Role of magnesium during spontaneous formation of a calcium phosphate layer at the periphery of a bioactive glass coating doped with MgO, *App Surf Sci* 2003;211: 89–95.
5. Pascual B, Vazquez M, Gurruchaga I, Goni I, Ginebra MP, Gil FJ, Planell JA, Levenfeld B, San Roman J, New aspects of the effect of size and size distribution on the setting parameters and mechanical properties of acrylic bone cements, *Biomater* 1996; 5: 509-516.
6. Di Gerlando A, Perini R, Dispensa di Macchine Elettriche.
7. Muhlethaler J, Biela J, Kolar JW, Ecklebe A, Core losses under DC bias condition based on Streinmetz parameters, *IEEE Trans Smart Grid* 2012; 27: 0885–8993.
8. Bretcanu O , Verne´ E, Coisson M, Tiberto P, Allia P, Temperature effect on the magnetic properties of the coprecipitation derived ferrimagnetic glass-ceramics, *J of Magn and Mag Mat* 2006; 300: 412–417.
9. Bickford LR, Ferromagnetic Resonance Absorption in Magnetite Single Crystals, *Phy Rev*, 1950;78: 449-457.
10. Song NN, Yang HT, Liu HL, Ren X, Ding HF, Zhang XQ, Cheng ZH, Exceeding natural resonance frequency limit of monodisperse Fe₃O₄ nanoparticles via superparamagnetic relaxation ,DOI: 10.1038/srep03161.
11. Oliveira JM, Correia RN, Fernandes MH, Surface modifications of a glass and glass-ceramic of the MgO-3CaO P₂O₅-SiO₂ system in a simulated body fluid, *Biomater* 1995; 16: 849-54.
12. Verné E, Bretcanu O, Balagna C, Bianchi CL, Cannas M, Gatti S, Vitale-Brovarone C, Early stage reactivity and in vitro behavior of silica-based bioactive glasses and glass-ceramics, *J Mater Sci Mater Med* 2009; 20(1): 75-87.

Results and Discussion Composite bone cement characterization

13. Verné E , Miola M, Ferraris S, Bianchi CL, Naldoni A , Maina G, Bretcanu O, Surface Activation of a Ferrimagnetic Glass–Ceramic for Antineoplastic Drugs Grafting. *Adv Eng Mater* 2010; 12: B309-B319.
14. Vitale-Brovarone C, Verne´ E, Robiglio L, Appendino P, Bassi F, Martinasso G, Muzio G, Canuto R, Development of glass–ceramic scaffolds for bone tissue engineering: Characterisation, proliferation of human osteoblasts and nodule formation. *Acta Biomater* 2007; 3:199–208.
15. Panseri S, Cunha C, D’Alessandro T, Sandri M, Giavaresi G, Marcacci M, CT Hung and Tampieri A , Intrinsically superparamagnetic Fe-hydroxyapatite nanoparticles positively influence osteoblast-like cell behaviour. *J of Nanobiotech* 2012;10:32.
16. Pareta RA, Taylor E, Webster TJ, Increased osteoblast density in the presence of novel calcium phosphate coated magnetic nanoparticles. *Nanotech* 2008; 19: 26-51.
17. Hayes JS, Khan IM, Archer CW, Richards RG. The role of surface microtopography in the modulation of osteoblasts differentiation. *Eur Cells Mater* 2010; 20: 98-108.
18. Hildebrandt B, Wust P, Ahlers O, Dieing A, Sreenivasa, G, Kerner T, Felix R, Riess, The cellular and molecular basis of hyperthermia. *Crit Rev in Onc/Hemat* 2002; 43: 33-56.
19. P. Yuan, Numerical analysis of temperature and thermal dose response of biological tissues to thermal non-equilibrium during hyperthermia therapy. *Med Eng & Phy* 2008; 30: 135–143.
20. Cui Y, Liu B, Xie J, Xu P, Michael Tsion HH, Zhang Y, The effect of hyperthermia on cell viability, oxidative damage, and heat shock protein expression in hepatic cells of grass carp (*Ctenopharyngodon idellus*). *J of Ther Biol* 2013;38:355-361.

Chapter 7

Results and discussion

Antibacterial characterization of SC45

7.1. SC45 doped with silver and copper

In this experimental part the synthesis and characterization of SC45 glass-ceramic doped with antibacterial ions is described. This modification is intended to prevent the infections than could be potentially generated into the bone after surgical resection of a tumor.

The synthesis of the antibacterial glass ceramic was carried out by two different approaches:

1) **Melting and quenching technique.** The antibacterial agent (silver or copper) is introduced into the glass in oxide form, with a modification of the glass ceramic chemical composition directly during its synthesis.

2) **Ion exchange in molten salts.** This technique permits the glass ceramic doping by a direct contact with a molten salt rich of antibacterial ions. The doping mechanism exploits the diffusivity principle for which the concentration of antibacterial ion in the molten salt come into the glass network with a consequent coming out of sodium ions.

The aim is to produce a multifunctional glass ceramic **antibacterial, bioactive and ferrimagnetic.**

7.2. Melting and quenching

7.2.1. EDS analysis of doped SC45 bulk and surface

Compositional, morphological, crystallographic analysis on antibacterial glass-ceramics was performed by using EDS analysis, FESEM / SEM microscope, and X-ray crystallography.

Using the electronic dispersion spectroscopy (EDS), by sampling different areas, it was possible to detect the atomic percentage of the elements present in the glass ceramics.

Tables 7.1, 7.2 and 7.3 show respectively, the results obtained by EDS analysis on SC45, SC45 3Ag and SC45 5Cu. Each sample is divided in two forms: powder and bulk. The production of powder sample considers the melting of inorganic oxides and the quenching in air with no further heat treatment and with a subsequently grinding of the powder. The second form is a bulk material, which undergo a heat treatment at 600°C for 12 hours after quenching, and then grinded. All the analyses were performed in triplicate and the values are expressed as a mean.

Results and Discussion Antibacterial characterization of SC45

SC45		
Element	Theoretical value (% at)	EDS Area (% at)
Na	25,4	29
Ca	14	12,9
Si	24	24,4
P	2,7	2,5
Fe	34	31,2

Table 7.1: Atomic percentage of SC45

The theoretical values of SC45 are comparable with the compositional EDS area performed on the sample. Any significance difference is noticed in the control sample.

SC45 3Ag			
Element	Theoretical value (% at)	EDS Area bulk (% at)	EDS Area powder (% at)
Ag	1,57	0,54	0,4
Na	20,58	19,35	22,47
Ca	14,62	16,02	13,97
Si	24,97	30,59	27,85
P	2,84	3,41	3,2
Fe	35,42	30,09	32,11

Table 7.2: Atomic percentage of the elements in SC45 3Ag

Table 7.2 reports the theoretical composition of SC45 3Ag and the experimental one (EDS) on bulk and powder samples respectively. It can be noticed that the theoretical amount of silver is higher than the experimental values both for bulk and powder material; however it must be considered that the experimental error is around 1%. No wide variations are noticed for the other chemical element.

SC45 5Cu			
Element	Theoretical value (% at)	EDS Area bulk (% at)	EDS Area powder (% at)
Cu	3,7	2,6	1,9
Na	25,8	27,1	37,3
Ca	9	9,1	6,7
Si	24,3	29,3	21,5
P	2,7	2,6	2,3
Fe	34,5	29,2	30,3

Table7.3: Atomic percentage of the elements in SC45 5Cu

The quantitative analysis (atomic percentages) of copper is reported in table 7.3. Taking into account the experimental error, the measure does not show any variation in the theoretical and experimental evaluations in powder and bulk samples. An important variability is reported for some elements, such as sodium, which varies from 25,77% to 37,32% in the powder sample.

In conclusion for both silver doped glass ceramic and copper doped glass-ceramic, it can be noticed that the atomic percentages of antibacterial agents are comparable with the theoretical predictions.

7.2.2. FESEM and EDS analysis on doped SC45

This section reports the morphological characterization of the SC45 3Ag and SC45 5Cu in bulk and powder form, compared to the control SC45. The control sample is not shown because already introduced in the first part of the chapter 6.

7.2.2.1. SC45 3Ag

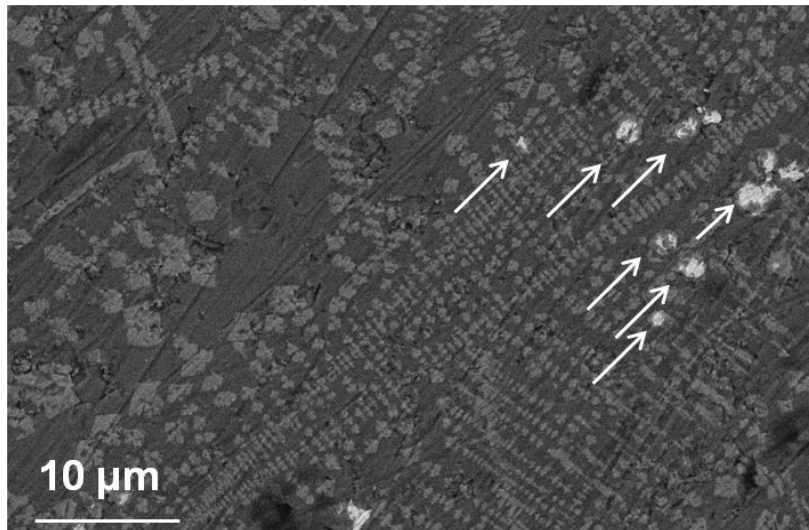


Figure 7.1: Morphological analysis of SC45 3Ag bulk

Figure 7.1 reports a bulk surface where a different morphology of crystals is noticed. Magnetite is the main one with some brilliant dots which is identified as silver micro-particles (indicated by white arrows).

Figure 7.2a, performed in backscattering, shows a large area of the SC45 3Ag bulk, where spindle-shaped crystals and circular silver particles, with a mean diameter of tens microns, can be seen. From preliminary evaluation on SC45 sample the spindle-shaped phase is hematite while the round particles are metallic silver. Figure 7.2b reports a magnification of a silver particle embedded into the glass matrix.

The backscattering detector application highlights the weight of the chemical element and for this reason evidences very well the difference between the glass and the silver particles. On surface samples some streaks can be noticed, due to the bulk cutting. Three different local zones of sample were analyzed with EDS technique: Figure 7.2c shows the composition of the amorphous phase of SC45. Figure 7.2d shows a sharp peak of silver.

Results and Discussion Antibacterial characterization of SC45

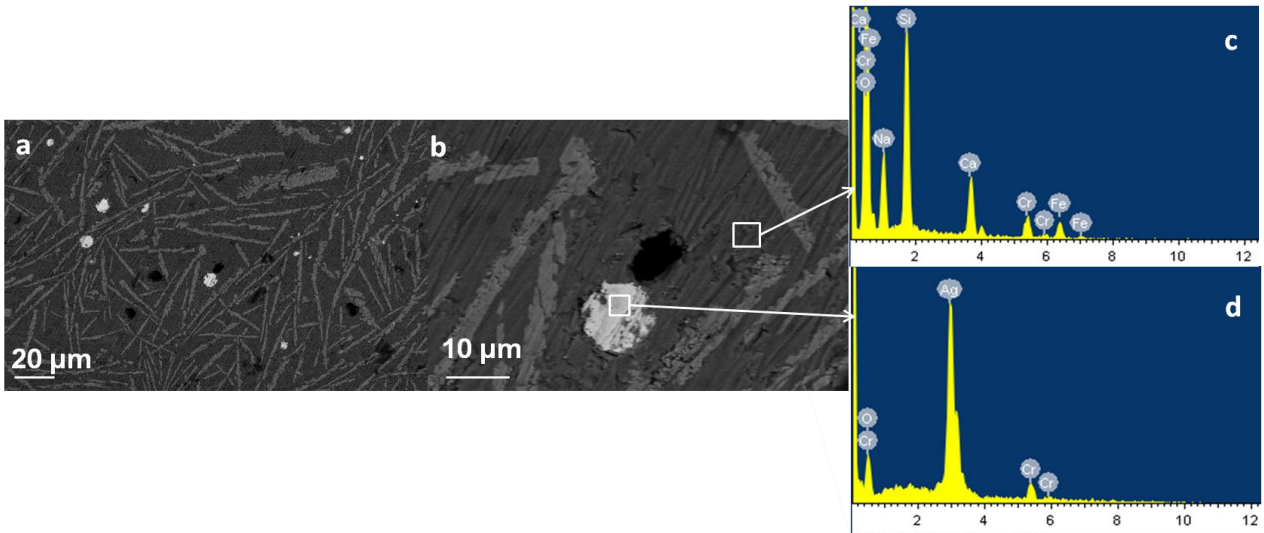


Figure 7.2: Morphological and compositional evaluations of SC45 3Ag bulk: a-b FESEM images, c-d EDS analysis.

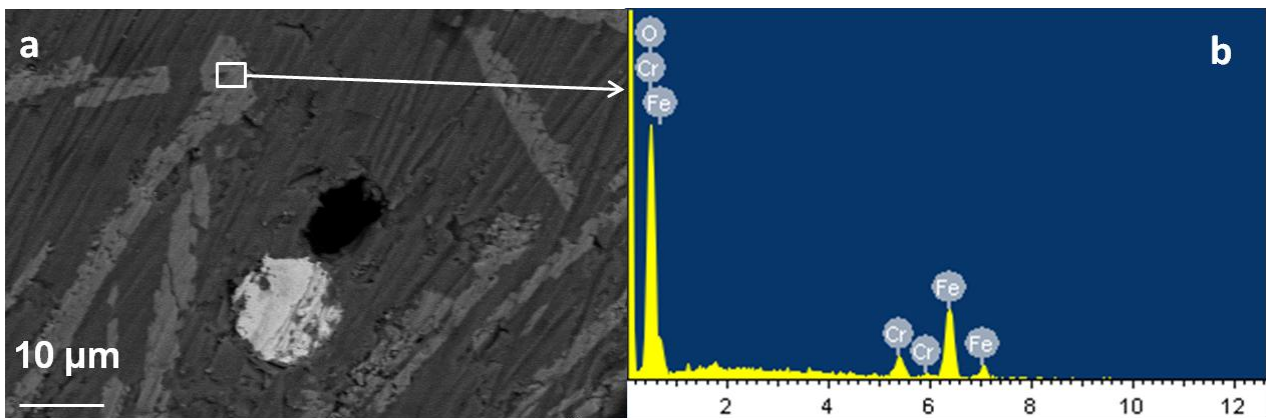


Figure 7.3: Morphological and compositional evaluations of SC45 3Ag bulk: a FESEM images, b EDS analysis.

The acicular shape in figure 7.3a is typical of hematite, an iron oxide with antiferromagnetic properties. Figure 7.3b reports compositional analysis of this phase where iron and oxygen peaks are prevalent. The chromium comes from the metallization process which permits a better conduction of the sample.

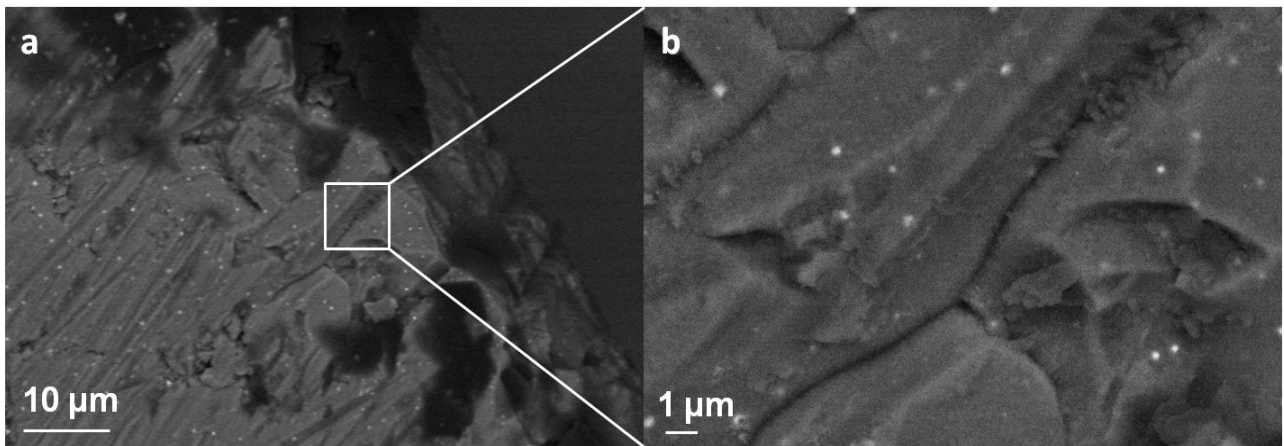


Figure 7.4: Morphological analysis of SC545 3Ag bulk

Figure 7.4a is taken on the outer edge of the bulk. The whole series of bright dots is attributed to the presence of crystals of silver nano-sized, the presence of silver nanoparticles could be useful for the antibacterial effect.

An acid attack was performed on Ag and Cu doped glass ceramics, in order to eroding the amorphous matrix and so permitting a better visualization of crystal phases included into the glass, highlighting the shape and the size of the different crystalline phases.

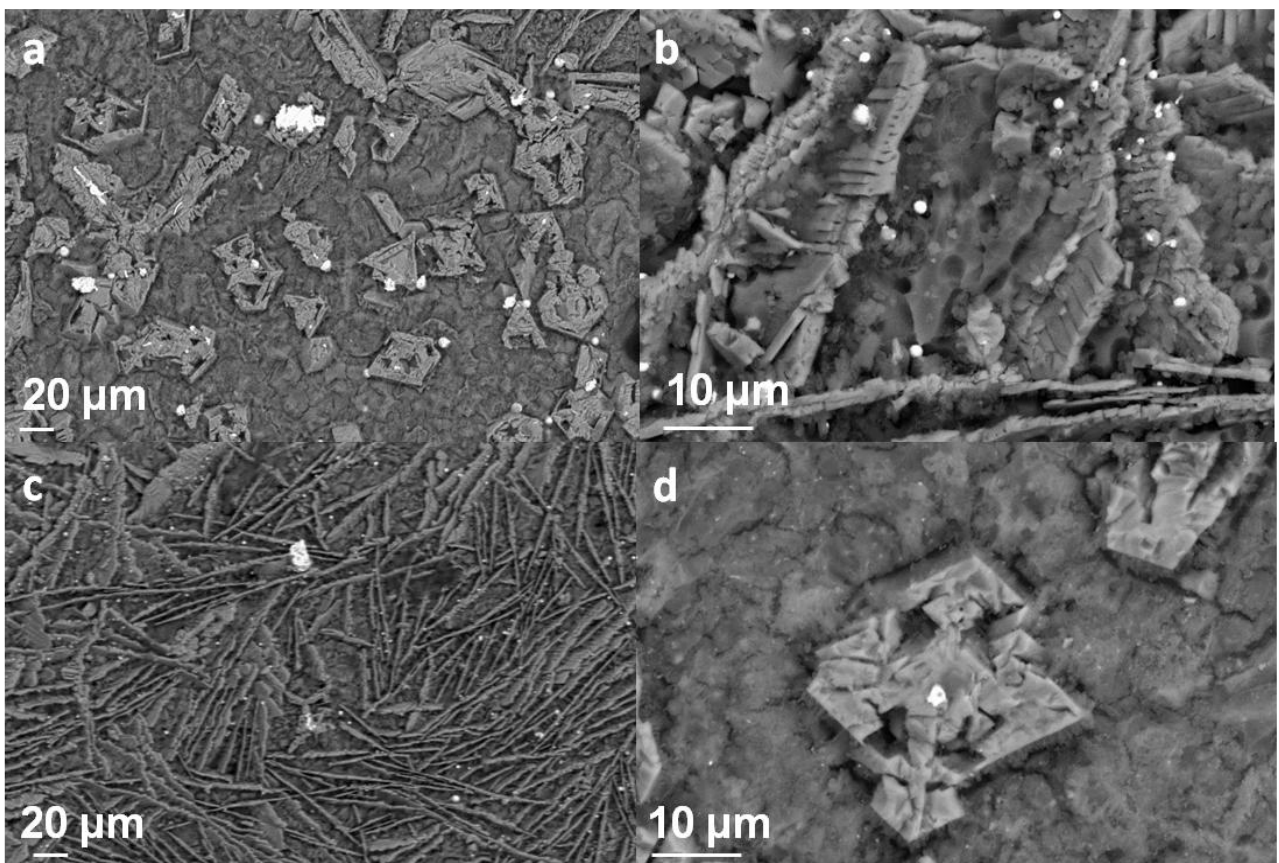


Figure 7.5: Morphological evaluation SC45 3Ag bulk after acid etching

Results and Discussion Antibacterial characterization of SC45

Figure 7.5 shows FESEM images of SC45-3Ag bulk subjected to this treatment. The presence of spherical dots of silver with different dimension is well evident in all images. Figure 7.5a is characterized by the presence of crystals, magnetite, with different morphology probably influenced by the presence of silver. Data from the literature report the action of silver as an agent that favors the nucleation of magnetite [1]. Figure 7.5a shows the presence of large silver particles (around 10-20 μm). Figure 7.5b evidences a prevalence of elongated crystals probably associate to hematite crystallization and smaller silver particles ($\sim 1 \mu\text{m}$). Figure 7.5c evidences a massive presence of elongated crystals of hematite. Figure 7.5d represents a crystal of magnetite with in the middle an Ag particle. As mention in [1] silver can act as a nucleate agent for magnetite .

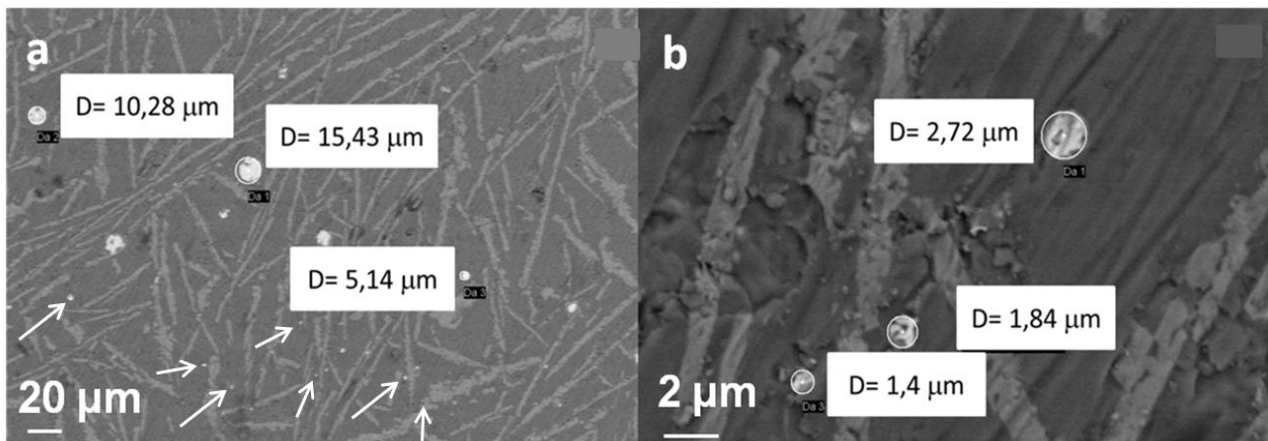


Figure 7.6: Measure of some silver particle diameter in SC45 3Ag bulk

The mean size of silver crystals is quite wide, the figure 7.6 evidences some diameters of silver particles. The biggest particles present diameters in the range of 1,4 to 15 microns, while the smaller ones can reach even some nanometers as highlights from the arrows in figure 7.6a.

Results and Discussion Antibacterial characterization of SC45

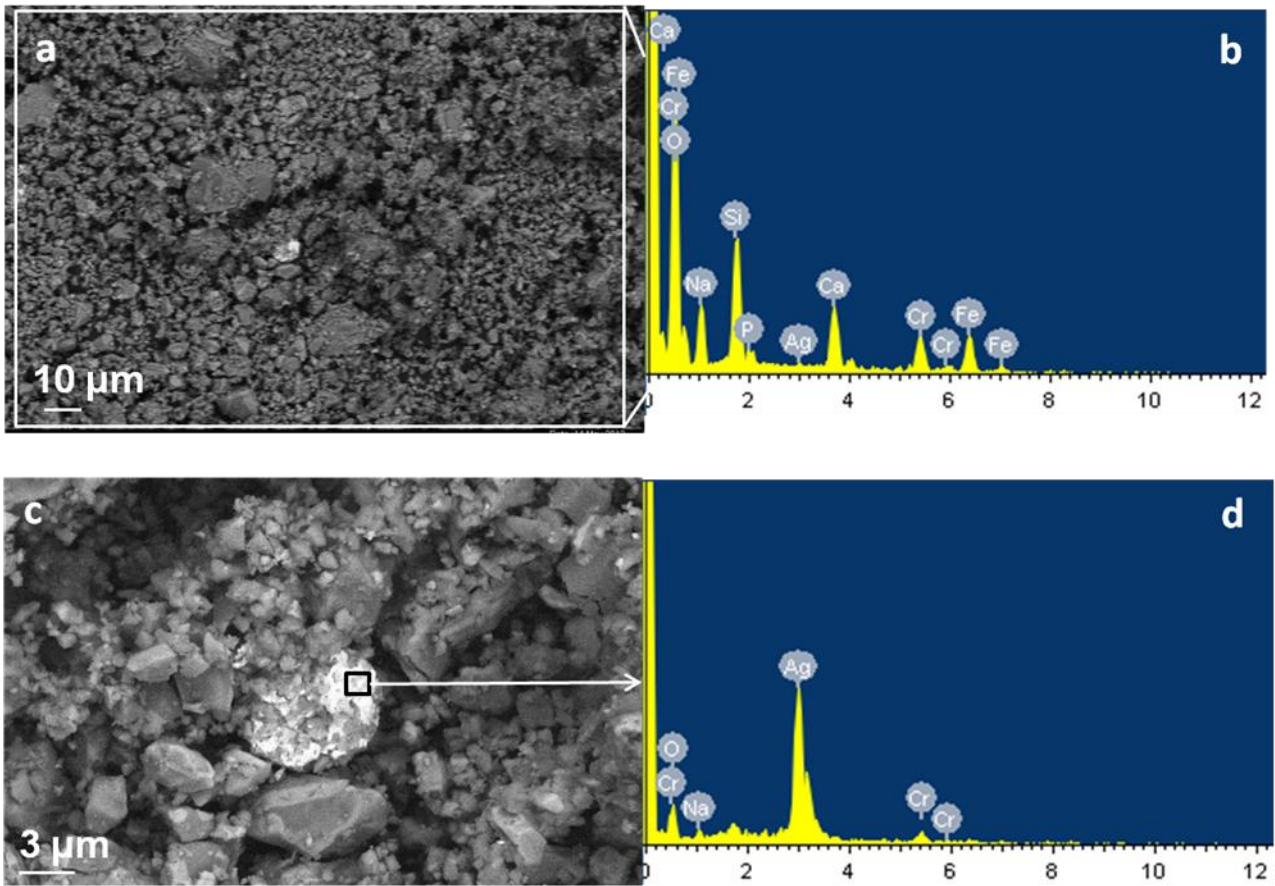


Figure 7.7: Morphological (a-c) and compositional (b-d) analysis of SC45 3Ag powder

Figure 7.7a reports the powder morphology of SC45 3Ag while 7.7b shows the compositional analysis of the sample surface. The presence of silver is confirmed in figure 7.7b and in the magnification in figure 7.7c. Due to the grinding process the silver particles appear not perfectly spherical

Figure 7.7d reports the compositional analysis of a bright particle: a sharp and high peak of silver is evidenced.

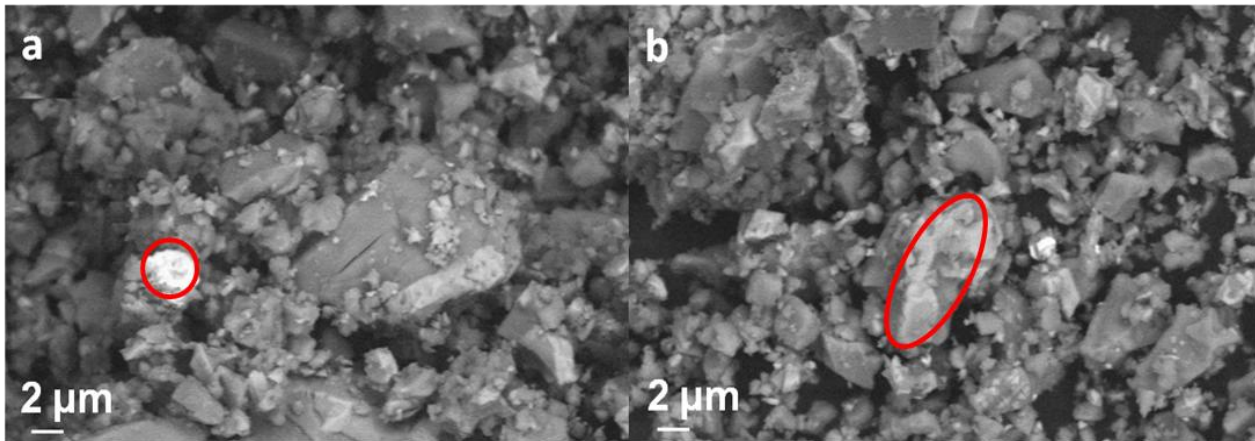


Figure 7.8: Morphological image of SC45 3Ag powder

Figure 7.8a shows SC45 3Ag powder sample. On the left it is possible to observe a circular bright dot with a mean diameter of 2 microns (red line). The other particles have different dimension but silver is seen only in this detail.

Figure 7.8b reports the sample SC45 3Ag powders. In the red line typical octahedral shape of a magnetite crystal into the glass matrix can be noticed. Even in this case the bright dots are silver. From FESEM investigation it appears that the main crystalline phase is magnetite with many silver precipitate with irregular shape and variable dimensions.

7.2.2.2. SC45 5Cu

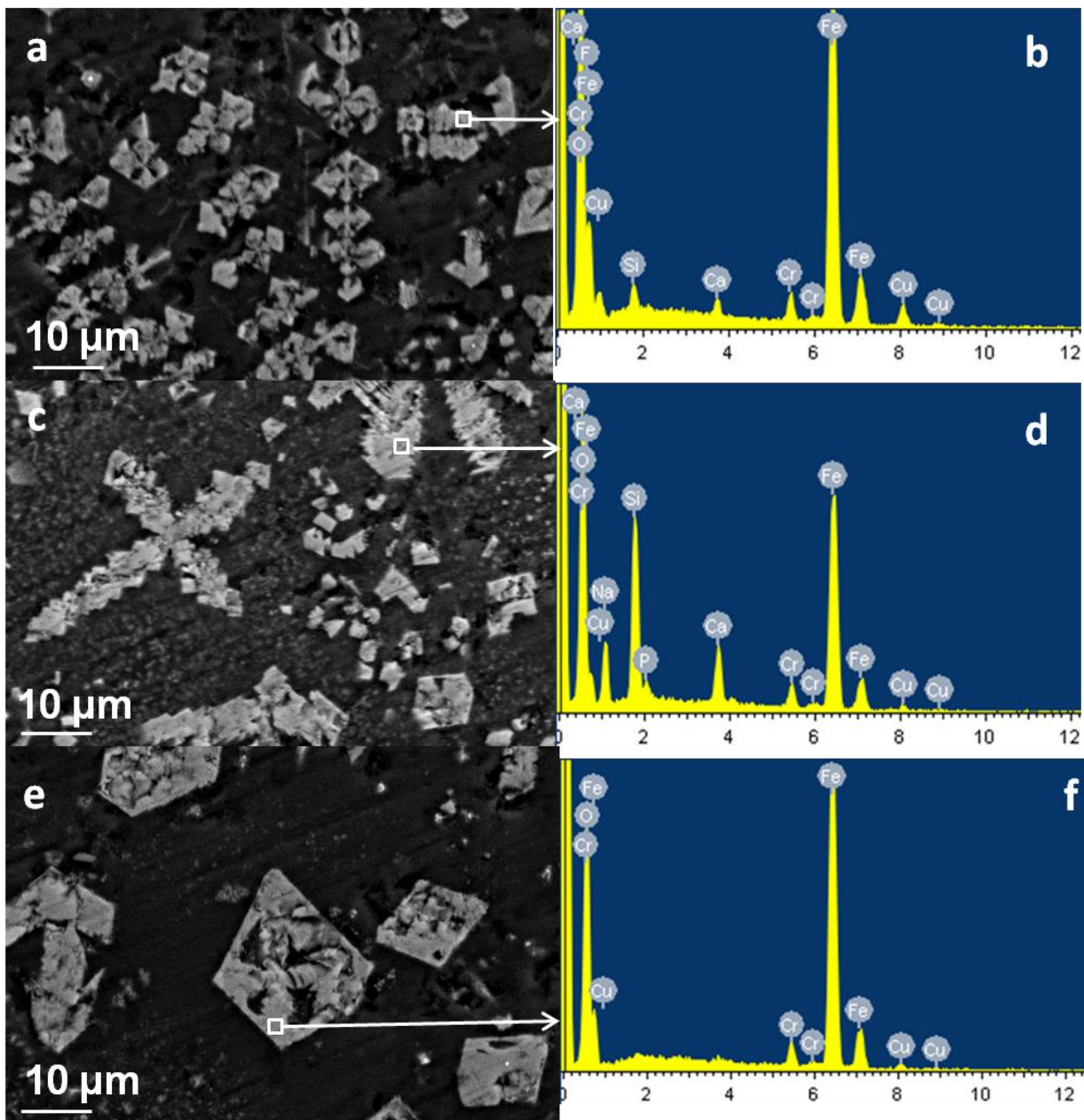


Figure 7.9: Morphological and compositional analysis of SC45 5Cu: a-c-e are bulk sample, b-d-f EDS analysis.

Figure 7.9a shows a bulk surface of SC45 5Cu where typical magnetite crystals are embedded into the glass matrix. The EDS analysis on a crystal in figure 7.9b evidences the presence of iron with a sharp peak, with the presence of copper, silicon, calcium, oxygen and chromium. Chromium comes from the metallization process for the FESEM visualization of the sample.

Figure 7.9c shows different crystalline phases which are nucleated in the glass ceramic. The crystals are cubic and with a cross-like shape. Even in this case the EDS analysis shows the

presence of large amount of iron with a small quantity of copper. Even the glass matrix elements are present: calcium, silicon, sodium and phosphorus.

Figure 7.9e shows some crystals which can be identified as magnetite. The EDS analysis evidences a very large amount of iron with a very low quantity of copper with no bio-glass compounds. It is supposed that the copper ions entered into the magnetite unit cell creating modified crystals [3].

As for SC45 3Ag even for SC45 5Cu bulk an acid attack was performed, in order to show the three dimensional structure of nucleated crystalline phases.

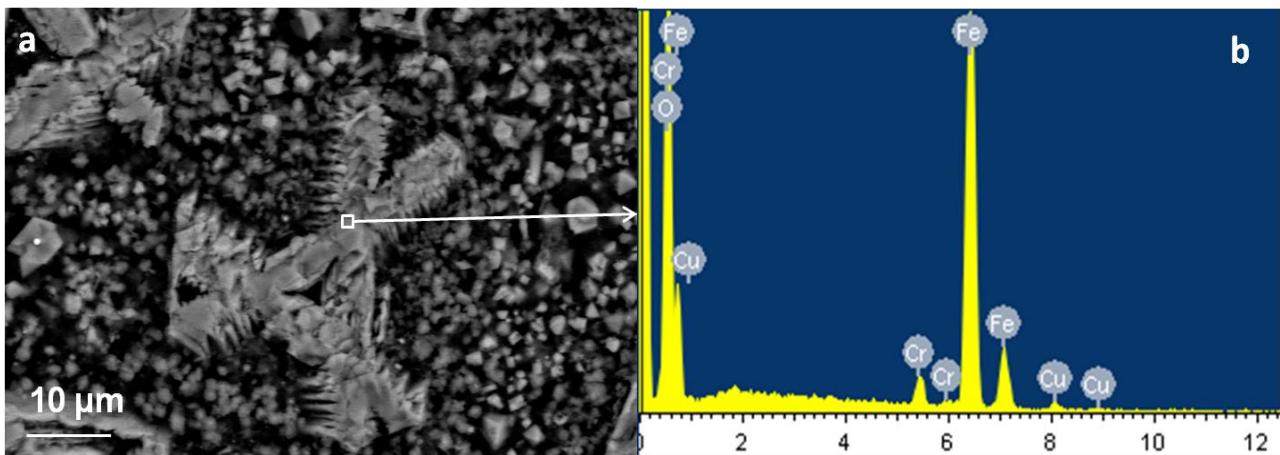


Figure 7.10: Morphological analysis on SC45 5Cu bulk (a), compositional analysis on crystalline phase after etching (b).

Figure 7.10a highlights very well the morphology of a crystal with a cross shape included in an eroded glass ceramic matrix. The shape of this crystalline structure is far from magnetite one; moreover the EDS analysis (figure 7.10b) evidences the presence of copper in this crystalline phase.

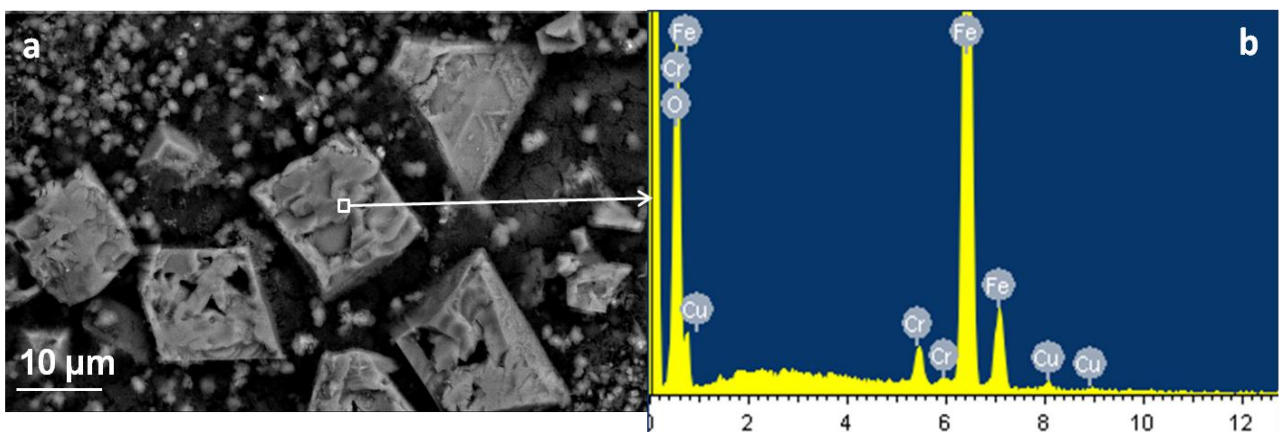


Figure 7.11: Morphological analysis of SC45 5Cu bulk (a), compositional analysis on some crystalline phase (b) after etching

Results and Discussion Antibacterial characterization of SC45

Even in figure 7.11a crystals with shape and morphology very far from magnetite are present. The presence of copper has influenced the nucleation of them. The local EDS analysis, reported in figure 7.11b shows a great amount of iron and the presence of copper.

Small particles near bigger crystals may be an artifact due to the glassy matrix partially corroded by the acid solution.

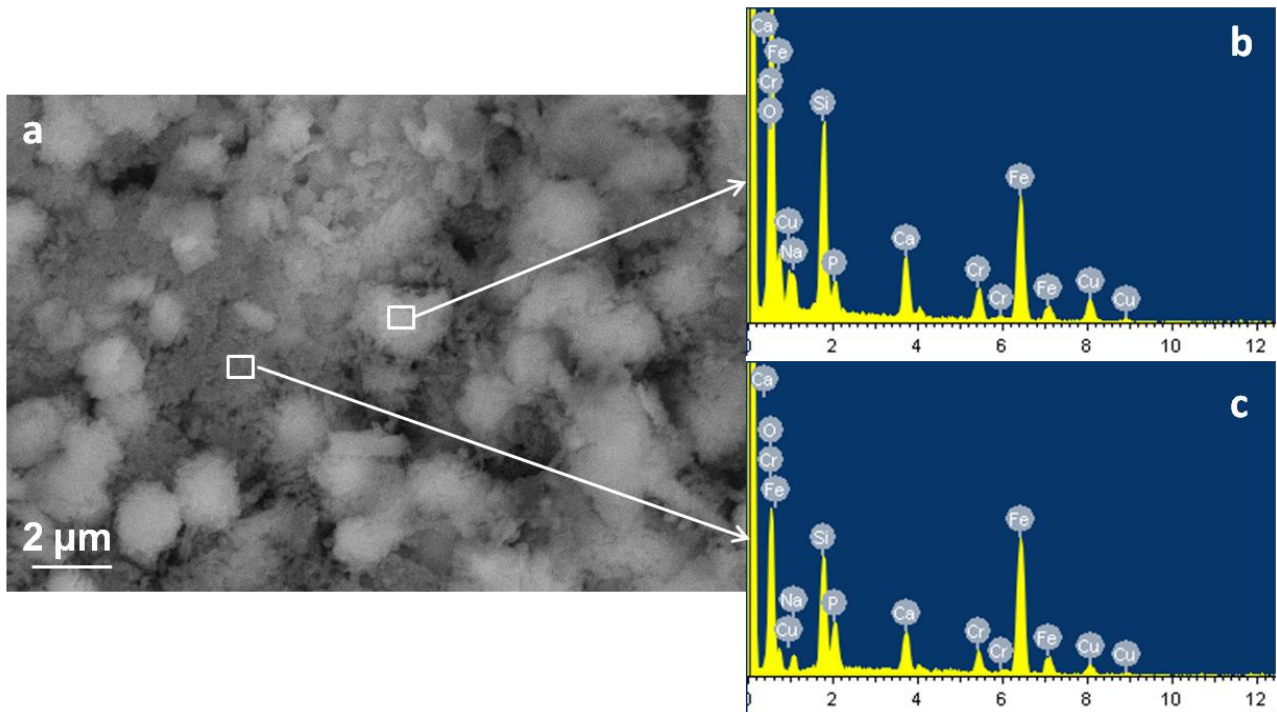


Figure 7.12: Morphological analysis of SC45 5Cu bulk (a), compositional analysis (b-c) after etching

Figure 7.12 reports a morphological and compositional analysis of the glass ceramic matrix. Figure 7.12b shows the composition of an amorphous zone of glass ceramic where there aren't crystalline phases. The spectrum reports a high amount of silica and iron together to all the other components of the glass ceramic. The presence of copper is also demonstrated. This is an encouraging result because confirms the presence of the antibacterial agent in the glass ceramic matrix. Another compositional analysis is performed in another point of the amorphous matrix and the spectrum detects a decrease of silica but almost the same amount of iron and copper. The presence of iron in the amorphous matrix confirms that a certain amount of iron ions do not take part in the magnetite nucleation and remain as intermediate in the glass network.

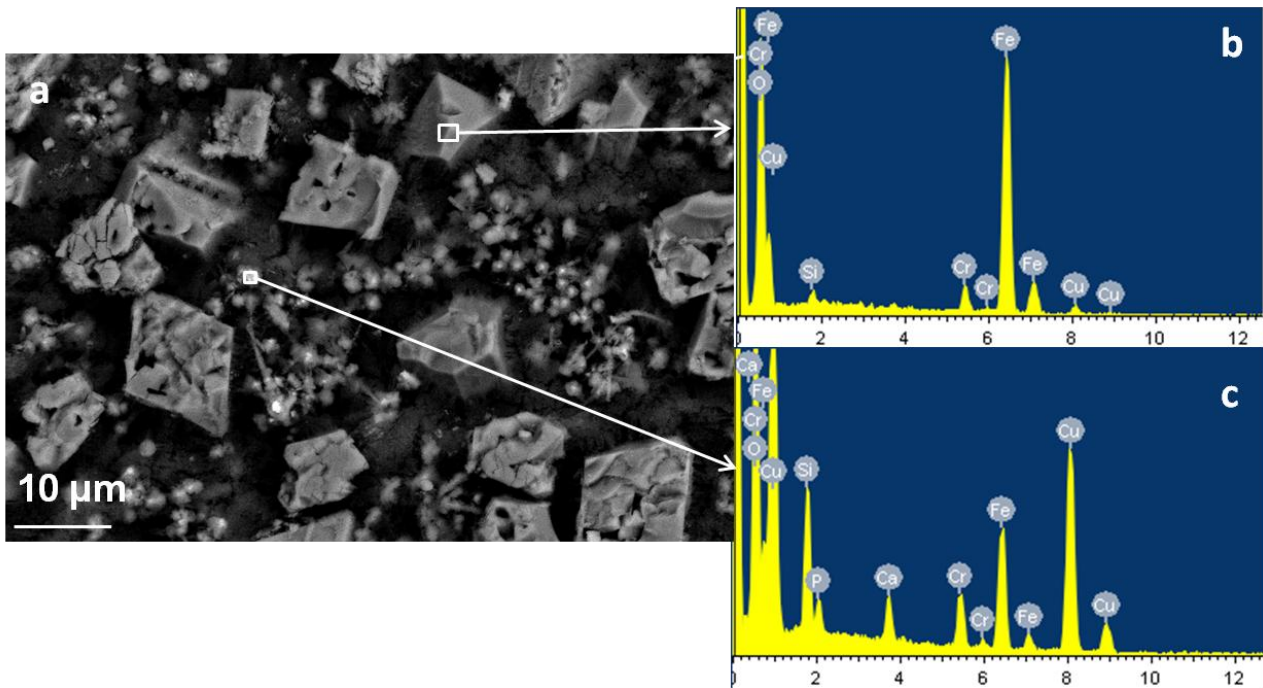


Figure 7.13: Morphological analysis of SC45 5Cu bulk (a), compositional analysis on some precipitates (b-c) after etching

Figure 7.13a evidences the morphology of crystals with a well defined 3D structure. Two EDS analyses are performed in two points of the sample. The first reports the compositional of a crystal with a very high quantity of iron, oxygen and copper. In the second local compositional analysis the presence of a high amount of copper is detected. This implies a possible presence of copper nanoparticles. The presence of the other glass ceramic elements is due to the penetration depth of the electron beam which penetrates (about 1 micron) into the sample.

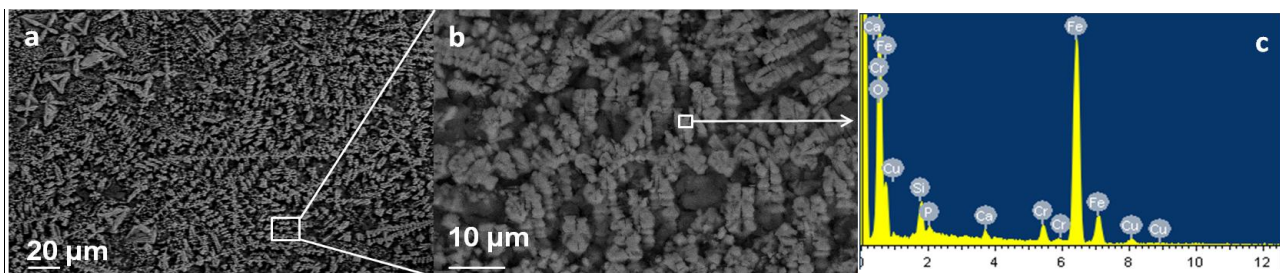


Figure 7.14: Morphological analysis of SC45 5Cu bulk (a-b), compositional analysis (c) after etching

Figure 7.14a reports several columnar magnetite crystals presented with very fine dimensions. Figure 7.14b evidence a magnification where the magnetite crystals have octahedral shape and they are assembled along a columnar line. The EDS analysis shows, as expected, the present of a high amount of iron and oxygen with traces of elements of amorphous phase and copper.

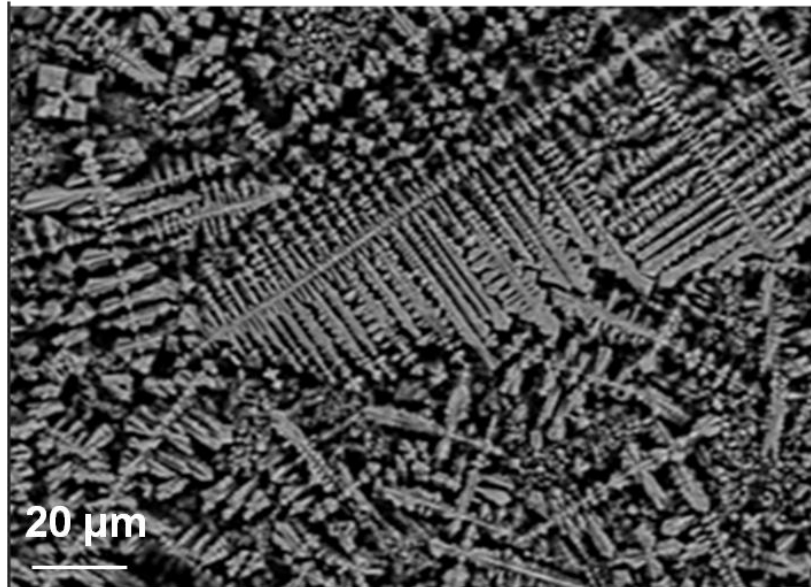


Figure 7.15: Morphological analysis of SC545 5Cu bulk after etching

Figure 7.15 shows several colonies of ordered nucleated crystals of magnetite into the bulk sample. The image shows a very wide size and shape of different nucleated Fe_3O_4 crystals.

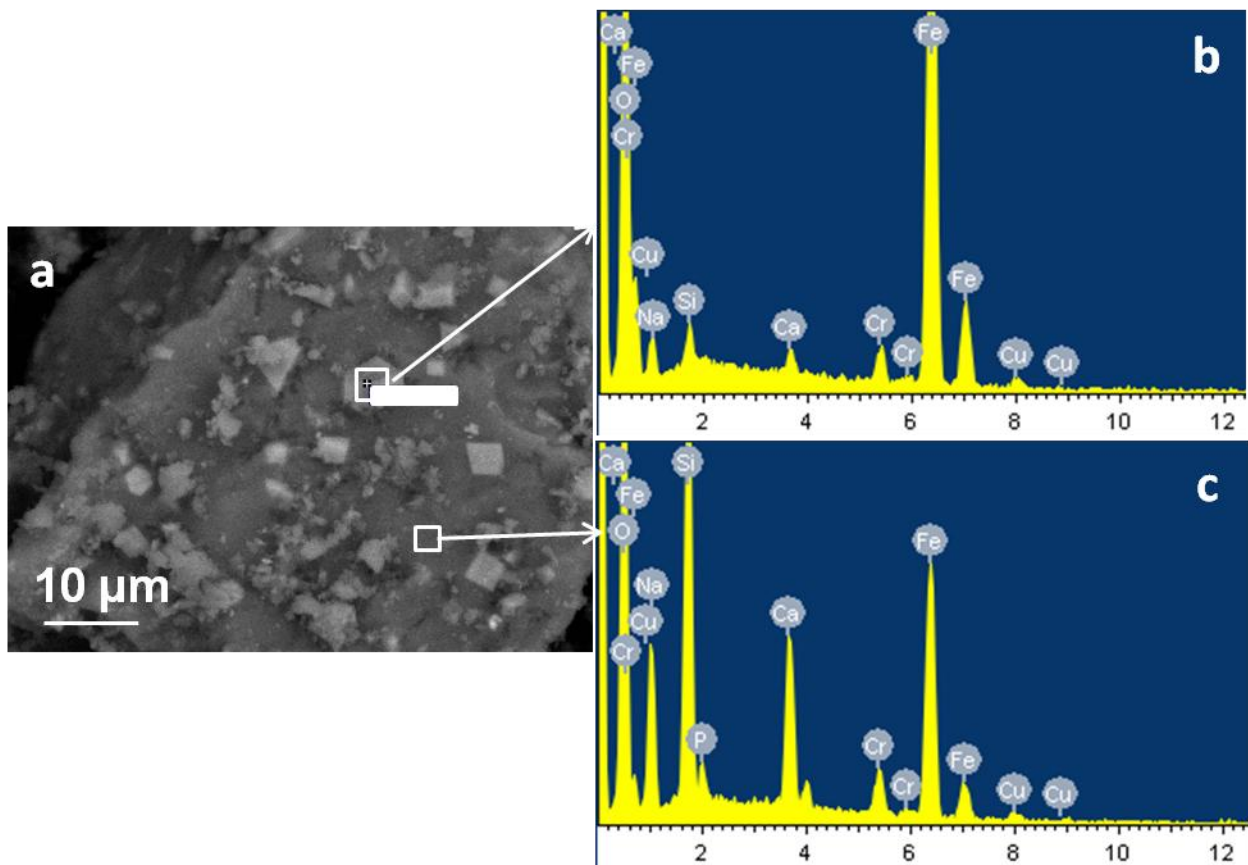


Figure 7.16: Morphological analysis (a) and compositional evaluation (b,c) of SC45 5Cu powder

Results and Discussion Antibacterial characterization of SC45

Figure 7.16a shows a low magnification of SC45 5Cu powder. EDS analyses reveal that copper is probably present both in the glass matrix and in the magnetite crystal. Figure 7.16b-c reports two zones in which a local EDS are performed. In figure 7.16b there is a high and sharp peak of iron with low amount of copper, while in figure 7.16c the compositional analysis shows high peaks of silicon, sodium, phosphorus and calcium typical of the glass matrix.

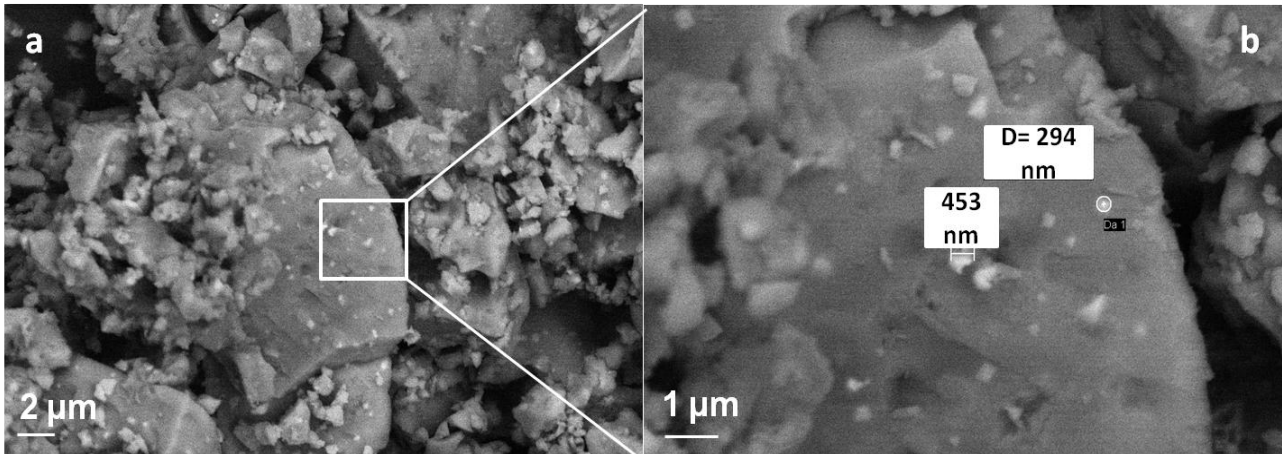


Figure 7.17: Morphological analysis (a, b) of SC45 5Cu powder

Figure 7.17 reports a sample of SC45 5Cu in powder form. As it can be seen the morphology is very different respect to the bulk sample. Several nanoparticles are present in figure 7.17a. The magnification in figure 7.17b evidences the shape and dimension of the nanoparticles. Some nanoparticles have an irregular shape, while others have a circular shape; their dimensions are hundreds of nanometres.

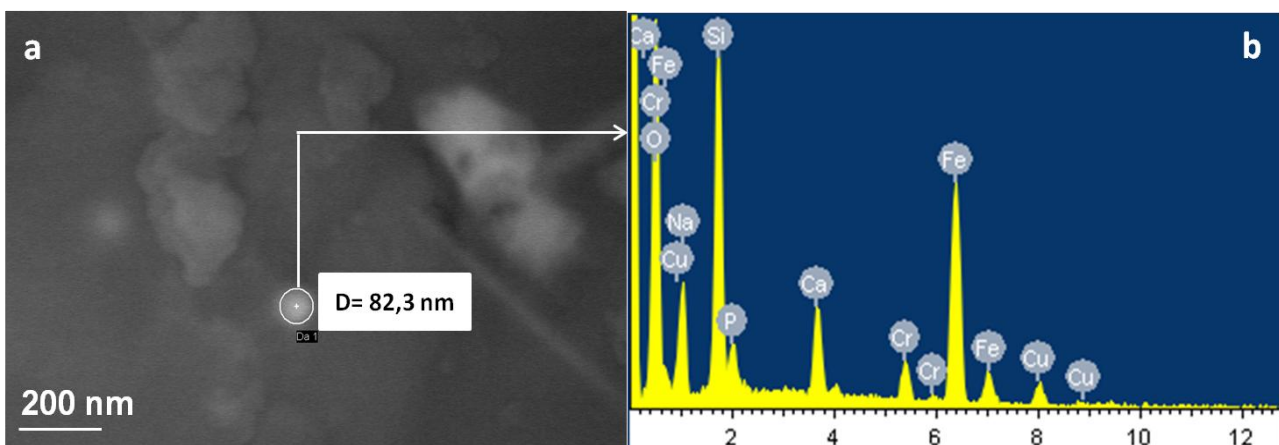


Figure 7.18: Morphological analysis (a) and compositional evaluation (b) of SC45 5Cu powder

Figure 7.18 a reports a magnification of a nanoparticle detected on a SC45 5Cu powder sample with a circular shape and a diameter of 82,3 nm. The compositional analysis performed locally evidences the presence of a higher copper amount.

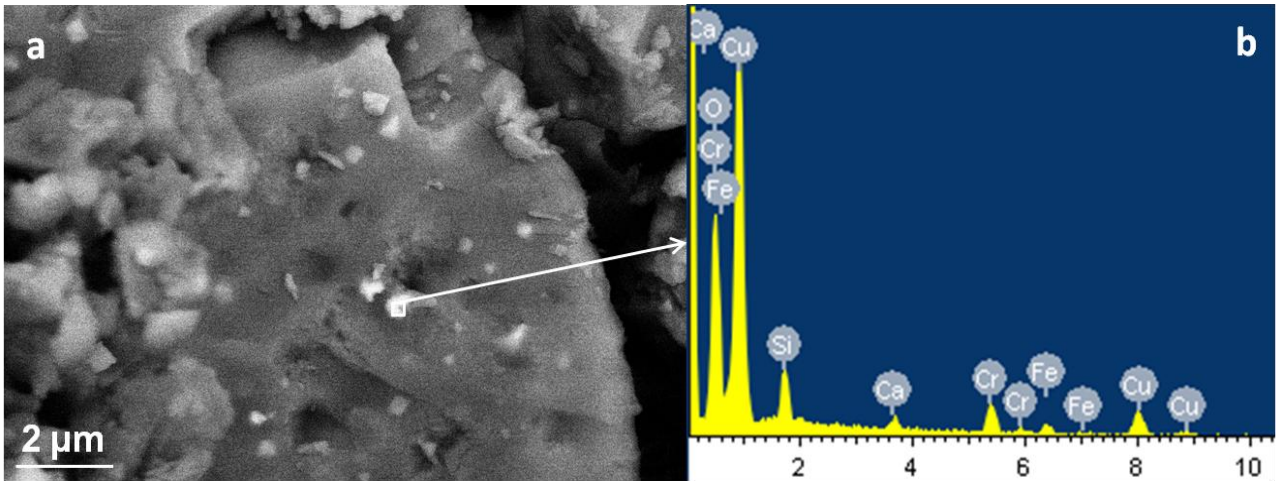


Figure 7.19: Morphological (a) and compositional analysis (b) of SC45 5Cu powder

Image 7.19 highlights the presence of a probable nano-sized copper particle in the glass matrix. EDS shows the presence of high copper peaks respect to the peaks of glass ceramic elements. In conclusion, in the SC45 5Cu samples copper seems to be present as nanometric particles or it is embedded in the glass network in ionic form .

7.2.3. XRD analysis

X-ray diffraction spectra of the glass ceramics doped with silver and copper are presented in the following section, together with the identification of crystalline phases nucleated into the glass ceramics.

For each graphic the legend for the identification of the sample is shown.

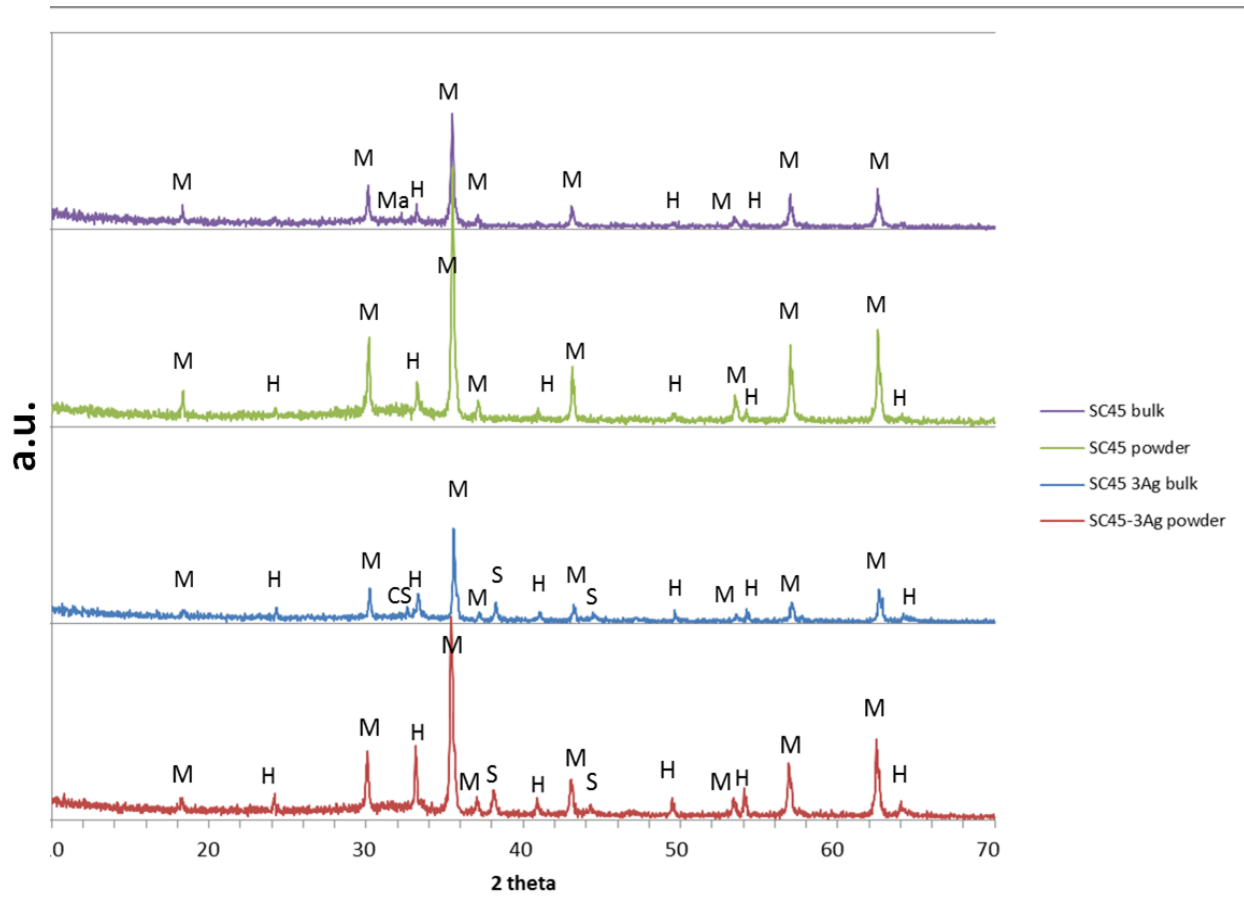


Figure 7.20: X-ray diffraction of SC45 3Ag powder , SC45 3Ag bulk, SC45 powder and SC45 bulk. The crystallographic peaks are identified with M magnetite, H hematite , Ma maghemite, CS calcium silicate , S metallic silver.

Figure 7.20 presents a comparison among x-ray diffraction patterns of SC45 and silver-doped glass-ceramics in powder and bulk forms.

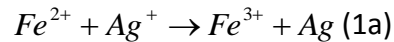
SC45 3Ag powder shows magnetite (Fe_3O_4), hematite (Fe_2O_3) and metallic silver (Ag) as main crystalline phases, as already evidenced in the FESEM morphological analysis. A low quantity of hematite is present in all analyzed sample . This phase has not influence the next magneto thermic characterizations due to its antiferromagnetic property. The 3Ag bulk sample presents the same crystal phases of SC45 3Ag powder. A small amount of calcium silicate is also presents.

SC45 powder shows the characteristic peaks of magnetite and hematite.

A hypothesis regarding the formation of silver metallic cluster in the glass ceramic is proposed. During the melting of the material at high temperatures, the oxides are liquid and not in a crystalline form an so the ions are available to react, if chemical specie with variable oxidation number, are present. The Fe^{2+} and Fe^{3+} ions contribute in a large amount to produce magnetite.

Results and Discussion Antibacterial characterization of SC45

However, a certain amount of Fe^{2+} ions in the glassy phase can react with the Ag^+ ions, according to the following redox reaction:



The Fe^{2+} is oxidized to Fe^{3+} while the Ag^+ is reduced to metallic silver.

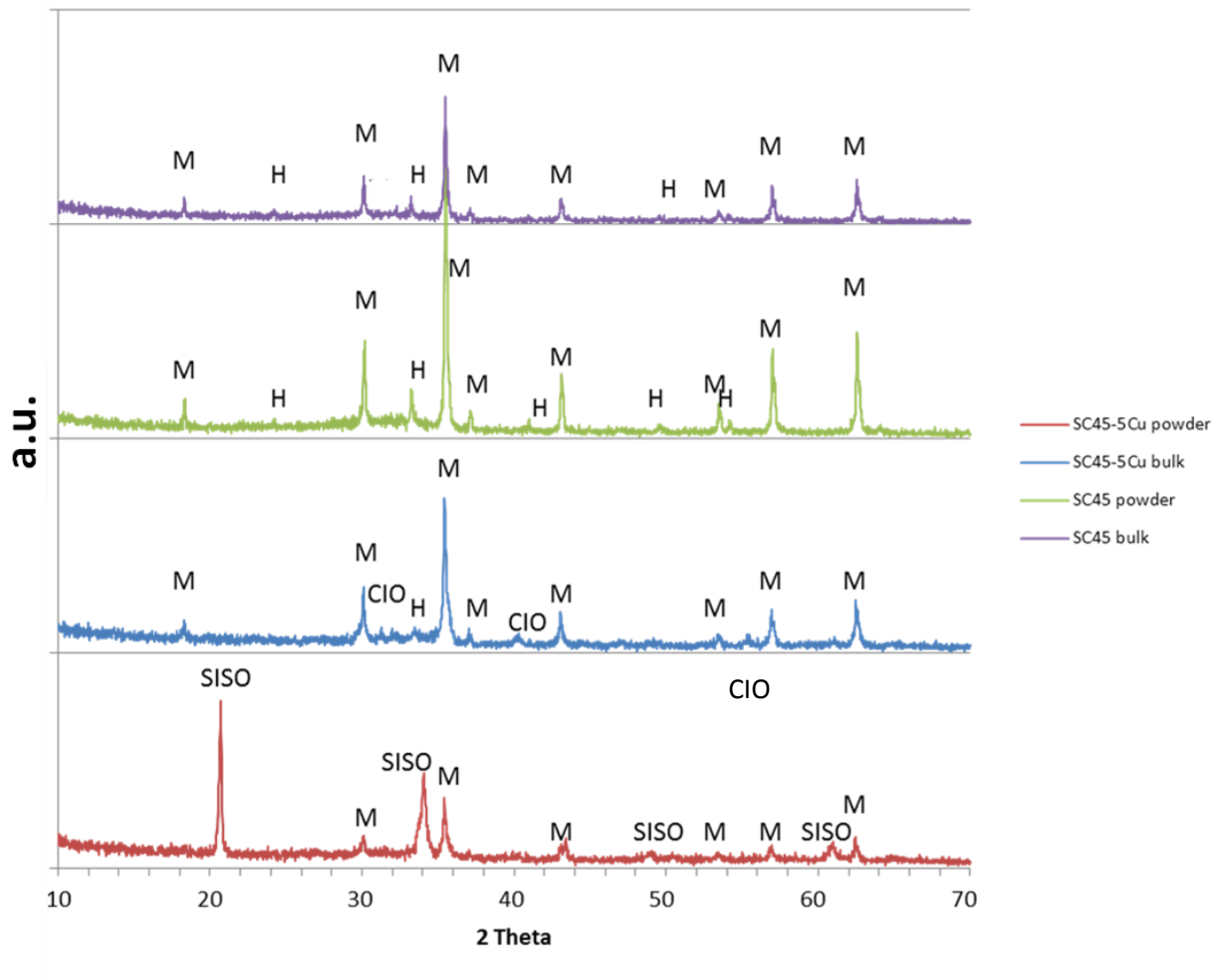


Figure 7.21: X-ray diffraction of SC45 5Cu powder, SC45 5Cu bulk, SC45 powder and SC45 bulk. The crystallographic peaks are identified with M magnetite, H hematite, CIO copper iron oxide ($CuFeO_2$), SISO sodium iron silicon oxide ($FeNaSiO_2$ in non-stoichiometric ratio).

Figure 7.21 presents a comparison among x-ray diffraction patterns of SC45 and copper-doped glass-ceramics in powder and bulk forms.

SC45 5Cu powder presents a very different spectra respect to the powder of pure SC45. The main peak of magnetite is very low and at 20,6 and 34,10 2θ angles an unexpected crystalline phase appears. Sodium iron silicon oxide in non-stoichiometric ratio nucleated in this glass ceramic. The presence of this phase could prevent iron from nucleation and crystallization as magnetite.